RESEARCH ARTICLE | FEBRUARY 25 2025

Large eddy simulation of a supersonic inlet turbine in a rotating detonation engine

N. Mushtaq ; C. P. Arroyo ; J. Dombard; F. Duchaine ; P. Strempfl; P. Gaetani

Physics of Fluids 37, 026138 (2025)
https://doi.org/10.1063/5.0255795

Physics of Fluids ARTICLE pubs.aip.org/aip/pof

Large eddy simulation of a supersonic inlet turbine in a rotating detonation engine

Cite as: Phys. Fluids **37**, 026138 (2025); doi: 10.1063/5.0255795
Submitted: 31 December 2024 · Accepted: 30 January 2025 ·
Published Online: 25 February 2025

View Online Export Citation CrossMark

N. Mushtaq,[1,a)] C. P. Arroyo,[2] J. Dombard,[2] F. Duchaine,[2] P. Strempfl,[2] and P. Gaetani[1]

AFFILIATIONS

[1]Laboratory of Fluid Machines (LFM), Department of Energy—Politecnico di Milano, Via Lambruschini 4, 20156 Milan, Italy
[2]CERFACS, 42 avenue Gaspard Coriolis, Toulouse 31057, France

[a)]Author to whom correspondence should be addressed: noraiz.mushtaq@polimi.it

ABSTRACT

A rotating detonation combustor (RDC) is an innovative technology with the potential to improve the efficiency of modern gas turbines. However, the highly unsteady and transonic flows generated by RDCs require advanced turbine designs, such as supersonic inlet turbines, to fully realize their benefits. This paper presents the first large eddy simulation of a complete supersonic turbine stage operating with RDC-representative inlet conditions. The investigation begins by evaluating the accuracy of Reynolds-averaged Navier–Stokes (RANS) simulations, widely employed for designing and optimizing supersonic inlet turbines. The strengths and limitations of RANS in capturing the complex flow physics of such systems are revealed. Aerodynamic losses within the turbine are quantified and compared with predictions from established mean-line design loss models. An entropy decomposition framework is then applied to uncover the dominant physical mechanisms of entropy generation and to identify regions of peak entropy production. The impact of RDC wave propagation through the stator and rotor blade rows is analyzed through phase–phase diagrams of phase-locked-averaged quantities, revealing key unsteady flow interactions. Additionally, the dominant modes characterizing the flow separation on the stator's suction side are detected with dynamic mode decomposition, and an accurate reduced-order model is developed with the state-of-the-art shallow recurrent decoder neural network. This work provides critical insights into the aerodynamic performance, loss mechanisms, and unsteady flow phenomena of supersonic inlet turbines in a rotating detonation engine (RDE). These findings pave the way for the practical implementation and continued advancement of RDE-integrated turbine technologies.

I. INTRODUCTION

Recent global developments have highlighted the persistent challenge of rising carbon emissions, despite increased climate efforts and growing investments in low-carbon energy.[1] Achieving the ambitious goal of net zero emissions will depend heavily on rapid improvements in energy efficiency and a significant rise in low-carbon energy. In this context, gas turbines integrated with rotating detonation combustors (RDCs) offer promising potential due to their higher efficiency[2,3] and compatibility with hydrogen.[4] The increase in efficiency is realized through the pressure gain induced by the detonation wave rotating and burning the fresh mixture in the combustion chamber.[5]

A successful integration of the RDC in the gas turbine architecture demands a severe redesign of the downstream components. The flow delivered by the combustor is highly fluctuating and transonic,[6] conditions that are unfavorable for turbine operation. Hence, current solutions foresee an accelerating or decelerating transition duct to connect the combustor with, respectively, a supersonic or subsonic inlet turbine. Each alternative has its advantages: supersonic inlet turbines extract substantial work in the first stage lowering the cooling requirements in the subsequent ones;[7] subsonic turbines require less redesign effort by optimizing conventional geometries for this specific application.[8,9] This work focuses on the supersonic configuration of the rotating detonation engine (RDE).

Nakata *et al.*[10] demonstrated through experiments that supersonic flow can be achieved without a geometrically converging section since the large heat release from detonative combustion induces thermal choking. Various duct shapes have been explored, with Braun *et al.* observing that smoothly diverging nozzles are the most effective in attenuating fluctuations.[11] Building on this insight, Mushtaq *et al.*[12] proposed a novel implementation of the method of characteristics to design optimal supersonic annular ducts for RDEs, featuring asymmetric and rotated hub and shroud walls.

Paniagua *et al.*[13] and Mushtaq *et al.*[7] developed mean-line design codes tailored for supersonic inlet turbines. During the preliminary design phase, careful attention must be given to prevent Kantrowitz unstarting[14–16] and collective shock unstarting[16] under all operating conditions.

Subsequently, several optimization procedures can be employed to enhance turbine performance. For instance, Sousa and Paniagua[17] optimized the supersonic blade profile, while Mushtaq *et al.* introduced techniques to optimize cascade solidity[7] and end wall geometry.[18]

The interaction between supersonic inlet turbines and the RDC has been numerically investigated using various levels of fidelity and approximations of real-engine operating conditions. Euler simulations have explored the influence of nozzle guide vanes on RDC flow structures.[19] Unsteady Reynolds-averaged Navier–Stokes (URANS) simulations with sinusoidal inlet fluctuations have been performed to assess the impact of inlet unsteadiness on blade aerodynamic performance[20] and unstarting phenomena.[21] Furthermore, time-resolved URANS simulations, using combustor-representative outlet conditions derived from an unfolded two-dimensional RDC model, provided insights into turbine stage performance.[22] A two-dimensional URANS analysis also examined the coupling between the supersonic turbine stage and the RDC.[23] In terms of higher-fidelity approaches, large-eddy simulations (LES) of the stator blade row were conducted to investigate blade damping capabilities under oscillating inflow[24] and shock-boundary layer interactions under steady inlet conditions.[25]

The current state-of-the-art research on turbine-RDC interaction has primarily focused on mid-fidelity simulations (URANS) of the entire turbine stage with RDC-representative inlet conditions, or high-fidelity simulations (LES) limited to the stator blades with simplified inlet conditions. This study advances the field by performing the first-ever LES simulation of the entire turbine stage using RDC-representative inlet conditions. This research makes two key contributions. First, it assesses the accuracy of Reynolds-averaged Navier–Stokes (RANS) simulations, widely used for designing and optimizing supersonic inlet turbines, by identifying their strengths and limitations in capturing the complex flow physics of these systems. Second, it provides a detailed aerodynamic analysis of a supersonic inlet turbine using advanced post-processing techniques, including entropy generation decomposition, phase–phase diagrams to analyze RDC-wave interactions with the downstream cascades, and reduced-order modeling of flow separation on the stator suction side. These methods, which have not been applied in previous studies (even for URANS), offer critical insights for the practical implementation and further development of RDE-integrated turbine technologies.

The paper is organized as follows: Sec. III provides the preliminary information necessary for this study. Specifically, a description of the supersonic transition duct and turbine geometry is presented in Sec. II A, while Sec. II B collects all the details regarding the computational flow model. In Sec. III, the overall performance metrics, the axial trends, and the flow fields in the blade-to-blade and axial planes from the RANS simulation are compared to the LES with steady and RDC-representative inlet conditions. Section IV focuses on aerodynamic losses. Overall loss values derived from CFD simulations are compared to predictions from mean-line design loss models. Additionally, the entropy decomposition framework proposed by Zhao and Sandberg[26] is applied to identify the dominant mechanisms of entropy generation and the regions where entropy production is most significant. Unsteady flow interactions within the supersonic turbine are explored in Sec. V. In Sec. V A, phase–phase diagrams of phase-locked average quantities reveal the propagation of the RDC wave through the stator and rotor blades. Section V B analyzes flow separation on the stator's suction side using dynamic mode decomposition[27] and introduces a reduced-order model based on a shallow recurrent decoder neural network.[28]

II. PRELIMINARIES

A. Supersonic inlet turbine and transition duct geometry

Figure 1 provides an overview of the transition duct and turbine geometry. It is important to emphasize that the configuration simulated here is the outcome of an extensive design process that involves advanced methodologies and targeted optimization procedures. This makes the

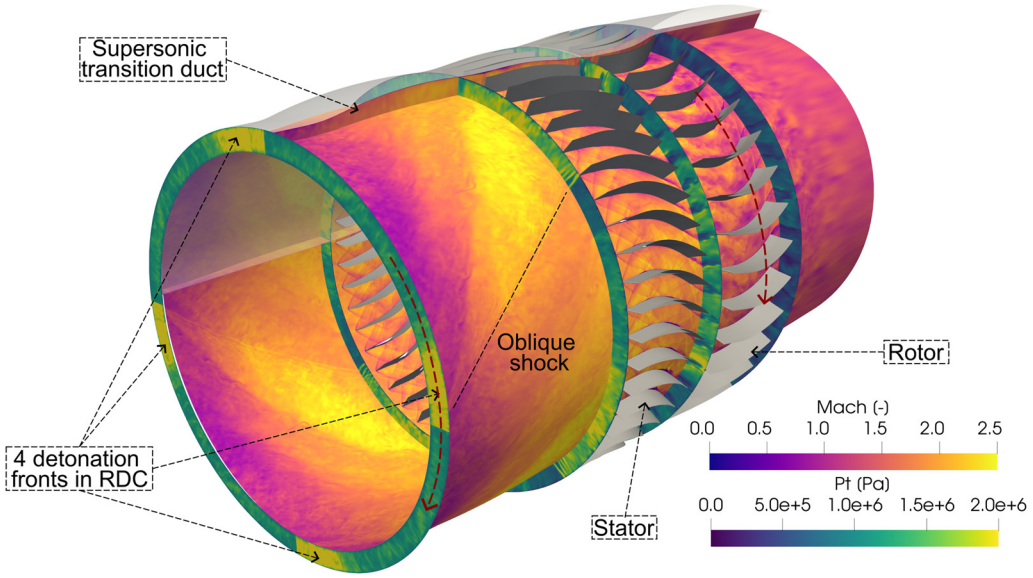

FIG. 1. Overview of the transition duct and supersonic inlet turbine geometry positioned downstream of the RDC. The Mach number field is displayed on the mid-height and meridional planes, while the total pressure field is depicted on four axial cross sections.

LES particularly valuable, as the detailed aerodynamic analysis is conducted on a geometry that represents the designers' best efforts to create an optimized machine for this specific application. Section II A briefly outline the key steps of the design process leading to this configuration.

The supersonic transition duct was designed with a novel implementation of the method of characteristics (MOC) for the generation of annular ducts with asymmetric and rotated hub and shroud walls.[12] A boundary layer code is coupled with the MOC to estimate boundary layer growth on the end walls and correct the shape accordingly. Parametric analysis carried out with a one-dimensional reduced model[29] of the duct suggested an outlet Mach number of 2, aimed at reducing angle fluctuations at the stator inlet. This value represents a compromise between key design factors: higher Mach numbers minimize incidence angle and ensure sufficient margin from unstarting phenomena, while lower Mach numbers minimize shock losses within the turbine. For a detailed description of the transition duct design methodologies, refer to Mushtaq *et al.*[12]

The preliminary design of the supersonic inlet turbine was carried out using a mean-line code specifically developed and verified for these machines.[7] The design point was selected based on parametric analyses, which showed that turbine efficiency increases at lower flow coefficients and higher stage loading coefficients. The stator inlet Mach number is 2, and the rotor relative inlet Mach number is 1.5, while the axial Mach number remains supersonic throughout the machine.

The supersonic stator and rotor profiles were generated with the "vortex-flow" method, which is a specific method of characteristics developed by Goldman and Vanco.[30] As the MOC profile has zero thickness at both the leading and trailing edges, the upper and lower surfaces were offset by the desired thickness; then, the edges were closed with high semi-axis ratio ellipses, a solution proven to enhance aerodynamic efficiency in supersonic cascades.[18] The pitch-to-leading-edge thickness ratio was optimized to reduce shock losses, while the thickness value was chosen to accommodate internal and film cooling channels.

Turbine performance was further enhanced through optimization procedures. Optimal loading conditions for the stator and rotor were determined using an automated CFD-based approach, as no established loading criteria exist for these unconventional machines. The optimal number of stator blades was increased from 47 to 48, while the rotor blades were reduced from 37 to 36, achieving 90° periodicity; this adjustment is essential for lowering computational costs and making the simulation more affordable. Given that end wall losses play a significant role in the overall loss breakdown, evolutionary surrogate-based strategies were employed to optimize the turbine's meridional shape. For more details on the role of end wall shape optimization in supersonic inlet turbines, refer to the work of Mushtaq *et al.*[18] Finally, Table I presents the main quantities defining the turbine geometry.

TABLE I. Geometrical definition of the turbine.

Parameter	Symbol/units	Value
Inner radius	r_i (cm)	34.5
Rotational speed	ω (rpm)	11 577.0
Stage reaction	χ (-)	0.0
Chord length	c (cm)	20.0
Inlet angle (stator)	α_1 (°)	0.0
Outlet angle (stator)	α_2 (°)	36.3
Inlet angle (rotor)	β_3 (°)	16.8
Outlet angle (rotor)	β_4 (°)	−30.1
Stator height at inlet	H_1 (cm)	6.4
Stator height at outlet	H_2 (cm)	8.3
Rotor height at inlet	H_3 (cm)	8.1
Rotor height at outlet	H_4 (cm)	9.6

B. Computational flow model

This work compares three types of simulations: a RANS simulation, an LES with steady inlet conditions, and an LES with unsteady inlet conditions representative of a rotating detonation combustor. It is important to note that LES results are compared with RANS instead of URANS, as URANS simulations are already too computationally expensive for the design phase. Typically, URANS are employed after the design is complete, shifting the focus to detailed aerodynamic analysis. However, with the increasing availability of computational resources, large-eddy simulations are expected to become the primary tool for analysis due to their superior accuracy. Sections II B 1–II B 3 provide detailed information on the numerical methods, boundary conditions, and grid generation employed in these simulations.

1. Numerical methods

Large-eddy simulations were performed using the AVBP code, a cell-vertex finite-volume solver developed by CERFACS.[31] Convective terms were discretized using the second-order in time and space Lax–Wendroff scheme,[32] chosen for its effective balance between computational efficiency and accuracy. The time integration was performed with an explicit scheme, maintaining the CFL number below 0.7 to ensure stability and convergence, which resulted in a time step of approximately 5.7×10^{-9} s. To achieve turbulence closure, the wall-adapting local eddy viscosity (WALE) sub-grid scale model, specifically developed for wall-bounded flows by Nicoud and Ducros,[33] was employed. Solver's ability to accurately simulate turbomachinery flows has been demonstrated in the work of Collado Morata *et al.*,[34] while its proficiency in handling detonation waves and supersonic flows in a RDC is showcased by Nassini *et al.*[35]

Meanwhile, RANS simulations were performed in Ansys CFX (Release 23.1),[36] which implements an element-based finite volume method with a pressure-based implicit coupled solver. The advection terms were discretized using a high-resolution total variation diminishing scheme;[37] this method applies a nonlinear blending factor, following the boundedness principles introduced by Barth and Jerspersen.[38] Turbulence closure was achieved through the k-omega shear stress transport (SST) model developed by Menter.[39] The Ansys CFX solver has been previously validated against four test cases:[16] the SOD shock tube, the inviscid supersonic wedge, the shock-wave/boundary layer interaction, and the bow shock wave shape generated by a probe placed in a supersonic converging–diverging nozzle.

Simulation convergence was considered achieved when the variation in integral quantities became negligible for both the steady-inlet LES and the RANS simulation. For the RDC-inlet LES, convergence was assessed by ensuring that the variation of relevant quantities from one period to the next remained minimal. Once convergence was established, the time-averaging process began: for the steady-inlet LES, averaging was performed over a period corresponding to a 90° rotor rotation (1.3 ms), while for the RDC-inlet LES, the results were averaged

over six full periods of the RDC wave (1.8 ms). The computational costs for the simulations were as follows: 750 CPU hours for the RANS simulation, 125 000 CPU hours for the steady-inlet LES, and 700 000 CPU hours for the RDC-inlet LES. These figures indicate why RANS simulations are primarily used for design and optimization, while LES is reserved for more detailed analysis during later phases.

2. Boundary conditions

The total pressure and total temperature assigned at the inlet of the transition duct are 15 bar and 2340 K, values typical of RDEs and high-pressure turbines.[2,13,40–42] In the steady inlet LES and in the RANS simulation, these values were maintained constant throughout the computation; meanwhile, in the RDC-inlet LES, these values are equal to the time-averaged mass-flow-averaged quantities.

The unsteady inlet conditions representative of the flow delivered by a rotating detonation combustor were built from a 3D LES carried out by Strempfl *et al.*[43] on the TU Berlin test rig geometry.[44] However, the RDC in Berlin is intentionally compact for experimental ease, while the supersonic inlet turbine was designed for a full-scale gas turbine integration operating at a 100 kg/s mass flow rate. Hence, some operations were necessary for mapping the flow field at the outlet of Berlin's RDC onto the annular inlet of the transition duct.

A conformal transformation was performed from the original 360° annulus to a 90° sector: the idea was to consider not one, but four co-rotating detonation waves in the combustor (Fig. 1). In this way, it is possible to drastically lower the computational cost by simulating only a quarter of the domain, (without this expedient, the full-annulus simulation would have required a mesh size of 1.2×10^9 cells and an estimated 3×10^6 CPU hours). This strategy is also well-supported by various studies in the literature showing that as the mass flow rate increases, the number of detonation waves rises, with up to nine waves observed in some cases.[4]

The Mach field, the flow angles, and the detonation wave speed were kept from Strempfl's simulation, while the non-uniformities in pressure and temperature were shifted with an iterative procedure to match the target value of average total pressure and temperature. An additional complication arises from the fact that the RDC LES employs wall modeling at the end walls, whereas the transition duct and turbine are wall-resolved (as discussed in Sec. II B 3). Directly interpolating the flow fields onto the transition duct inlet would result in inaccurate boundary layer profiles. To correct this, momentum and thermal boundary layers were manually constructed for each snapshot. Free-stream quantities were first extracted using Stratford and Beavers' correlations[45] to estimate boundary layer properties; then, the momentum and thermal layers were generated using the one-seventh power law and the simplified theory proposed by Bradshaw and Ferriss.[46] This approach also resolves any boundary layer inconsistencies caused by scaling the flow from a smaller to a larger section.

The unsteady inlet conditions were generated offline, creating a database of snapshots that the solver reads during the simulation.[48] The time interval between consecutive snapshots corresponds to a 0.12° rotation of the RDC wave (Fig. 1), and the database restarts after each full cycle of the detonation wave. It is important to note that while this method produces RDC-representative inlet conditions, the results are not identical to those from simulating a full-scale RDC. However, the generated flow fields include rotating detonation waves, realistic spatial and temporal non-uniformities, and turbulent inlet conditions. Therefore, the term "RDC-representative" was selected intentionally, as the authors believe the RDC-inlet LES effectively represents the real engine operation of the transition duct and the supersonic turbine in an RDE.

Combustion products are modeled as an ideal gas, with temperature-dependent variations of the thermodynamic properties handled with NASA polynomials.[49] Sutherland's law[50] is also applied to account for viscosity and thermal conductivity variation as a function of temperature.

The boundary conditions for both the LES and RANS simulations are consistent, with the primary distinction being that compressible LES simulations require at the inlet and outlet the Navier–Stokes characteristic boundary conditions (NSCBC) formalism to prevent wave reflections.[51] At the inlet of the transition duct, total pressure and total temperature are prescribed, while the outlet is set to supersonic flow. No-slip, adiabatic conditions are enforced on the blades and end walls, and periodic boundary conditions are applied at the lateral boundaries. In the RANS simulation, the interface between the stator and rotor is handled using a mixing plane, whereas the LES employs an overset grid approach.[52]

3. Domain definition and mesh generation

Two subdomains were defined for the mesh generation process, one for the stationary components (duct and stator) and one for the rotating ones. The domain starts at the inlet of the transition duct, while the outlet is located two chords downstream of the rotor's trailing edge.

Ansys TurboGrid (Release 23.1)[54] was used to generate a block-structured mesh with an HOH topology, consisting of hexahedral cells. The mesh density remains consistent throughout the transition duct and blade channels, with an expansion ratio applied in the outlet region to reduce computational cost. To ensure accurate boundary layer resolution, the y+ value is kept below 3 on both the end walls and blade surfaces. Figure 2 offers an overview of the mesh structure, including detailed close-ups of key areas. Additionally, it is important to note that the number of simulated blade channels varies across the three cases: 1 stator and 1 rotor channel for the RANS (with a mixing plane interface), 4 stator and 3 rotor channels for the steady-inlet LES, and 12 stator and 9 rotor channels for the RDC-inlet LES. Table II outlines the mesh size breakdown for each case.

A grid dependency study was carried out on the stator blade row to identify the optimal mesh size and characteristics necessary for accurately simulating these blade rows. Considering the option to reduce computational costs through wall modeling, three different approaches for wall treatment were explored with steady inlet conditions, as detailed in Table III. To assess which approach was most effective, a reference mesh consisting of 90 million cells for a single stator blade channel was generated. This mesh complied with the gold standard criteria for wall-resolved large eddy simulations established by Choi and Moin.[47] However, it is crucial to highlight that this level of resolution was not computationally viable for the entire domain, as it would necessitate a mesh size of around 3 billion cells.

In case (a), which applies a classical law of the wall to both the end walls and blades, performance is the poorest, with a 2.9% error in the mass-flow-averaged total pressure. Performance improves in case (b), where the blade boundary layer is resolved, but case (c) achieves the best accuracy, with errors in Mach number and total pressure under 0.3%.

The differences among the cases are not limited to integral quantities but also extend to flow features (Fig. 3). In the fully resolved 90×10^6 cell mesh, three primary flow characteristics are observed at the stator outlet: (A) and (B) represent two loss cores caused by

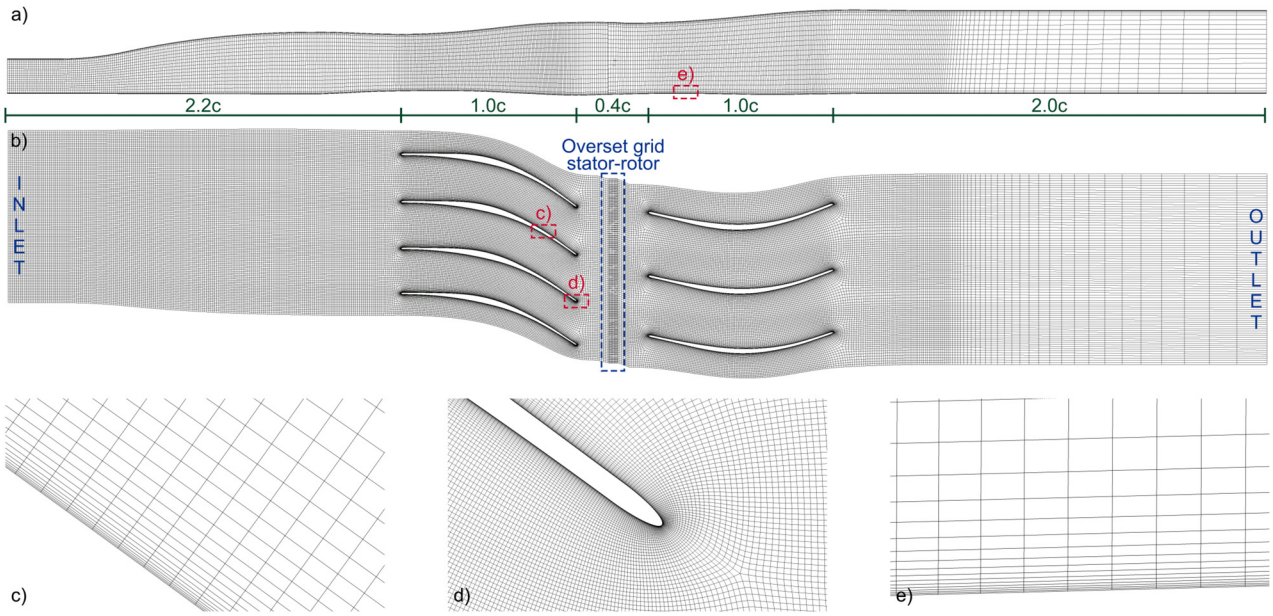

FIG. 2. (a) and (b) show the HOH topology used for meshing the domain, with only one out of every four grid lines displayed for clarity. (c)–(e) offer detailed views of the boundary layer on the stator suction side, the stator trailing edge, and the boundary layer at the hub wall, respectively.

TABLE II. Mesh size breakdown (in millions of cells) for the RANS simulation, the steady-inlet LES, and the RDC-inlet LES. The total mesh count includes the stator-rotor gap and the outlet region.

Simulation	Duct	Stator	Rotor	Total
RANS	5.4M	9M	12M	29M
Steady-inlet LES	5.4M × 4	9M × 4	12M × 3	100M
RDC-inlet LES	5.4M × 12	9M × 12	12M × 9	299M

boundary layer separation on the suction side, while (C) is the result of a horseshoe vortex at the leading edge. In case (a), the full wall modeling significantly overpredicts flow separation on the suction side, leading to a larger error in integral values. In case (b), resolving the blade boundary layer allows the loss cores to emerge, but the thicker end wall boundary layer increases blockage, causing the cores to move closer. However, in case (c), where both the end walls and blades are wall-resolved, the loss cores closely resemble those in the reference case in both size and position, and the secondary vortex induced by the horseshoe effect is also captured. Although the spanwise resolution in case (c) is closer to wall modeling than wall-resolving, it still provides accurate integral values and captures all relevant flow features. This result might be specific to the low-aspect-ratio blades employed in supersonic inlet turbines.

The index of resolution quality proposed by Celik *et al.*[53] was calculated to determine if 9 million cells per blade channel provide sufficient accuracy. This index is based on the Richardson extrapolation concept and requires the resolved turbulent kinetic energy from both a coarse and a refined mesh. Large-eddy simulations of the stator blade row under RDC-inlet conditions were used for this assessment, as these simulations are the most demanding due to the significant unsteadiness and turbulence in the flow. The mass-flow-averaged quality index consistently remains well above the recommended threshold of 80% along the stator channel, which indicates that the LES is well-resolved (Fig. 4). For the RANS simulation, the grid convergence index (GCI), proposed again by Celik *et al.*,[55] was calculated. The mixed-out[56] entropy production was selected as the reference quantity and the GCI from the fine to the

TABLE III. Comparison of four cases with varying resolutions for the blade and end wall boundary layers. The final row presents the criteria proposed by Choi and Moin[47] for wall-resolved large eddy simulations. x^+ is the axial direction, y^+ is the wall-normal direction, and z^+ is the third direction. The mass-flow-averaged total pressure and Mach number are calculated half chord downstream of the trailing edge.

Case	Mesh size	x^+ (-)	y^+ blade (-)	y^+ end wall (-)	z^+ (-)	$\frac{\tilde{p}_t - \tilde{p}_{t-d}}{\tilde{p}_{t-d}}$ (%)	$\frac{\tilde{M} - \tilde{M}_d}{\tilde{M}_d}$ (%)
Case a	9M	90	100	100	250	2.87	1.71
Case b	9M	90	< 3	100	250	1.85	0.77
Case c	9M	90	< 3	< 3	250	0.01	0.23
Case d (reference)	90M	90	< 1	< 1	25	...	...
Choi and Moin[47]	...	50–130	< 1	< 1	15–30	...	...

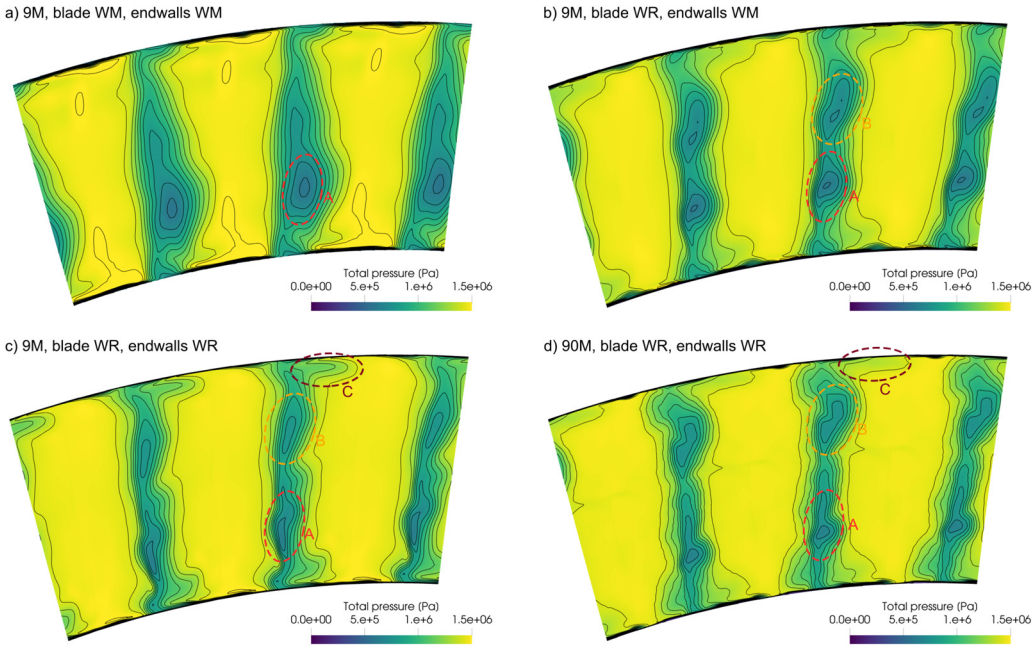

FIG. 3. Total pressure contours at an axial plane located half a chord downstream of the trailing edge, comparing the four cases presented in Table III. "WM" refers to wall-modeled, while "WR" indicates wall-resolved approaches.

medium mesh is 0.21%. After verifying that the 9×10^6 cell mesh of case (c) met all resolution criteria, the same mesh density and the same characteristics were employed to also generate the grids for the transition duct and the rotor.

III. COMPARISON BETWEEN LES AND RANS CALCULATIONS

This section presents an in-depth comparison between a RANS simulation, a LES with steady inlet conditions (referred to as "steady-inlet LES"), and a LES with unsteady inlet conditions representative of a rotating detonation combustor (referred to as "RDC-inlet LES"). This analysis is valuable, as RANS simulations are heavily employed in designing and optimizing supersonic turbines for RDEs. By identifying the limitations of RANS in comparison to LES, this analysis aims to inform and enhance future design efforts. The comparison begins with overall performance metrics, followed by a detailed examination of axial trends and flow feature distributions in both blade-to-blade and axial planes.

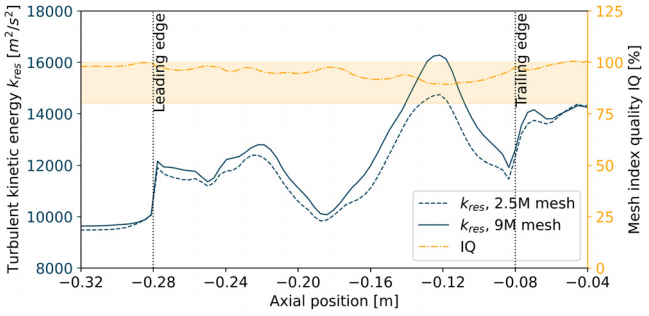

FIG. 4. Mass-flow-averaged resolved turbulent kinetic energy and index of resolution quality[53] along the stator.

Significant differences emerge among the three cases (Table IV). The RANS simulation predicts a total-to-total efficiency nearly 12 points lower than the steady-inlet LES. While increased losses contribute to this, the discrepancy is primarily due to a 4° reduction in flow turning, which reduces extracted work by 16% and directly impacts the total-to-total efficiency. In supersonic flows, even minor deviations in flow angles are critical due to the large variations in the tangential velocity component. While the RDC-inlet LES achieves similar work extraction to the steady-inlet LES, its efficiency is lower due to the additional entropy generated from the mixing of the highly unsteady and non-uniform inlet conditions.

The reduced flow turning in the RANS simulation might initially seem attributable to a more intense flow separation, but this is not the case. Flow angles across both the stator and rotor remain nearly identical up to the trailing edge in all three cases (Fig. 5), indicating that the deviation in the RANS simulation originates from trailing-edge flow physics. Figure 6 provides a close-up view of the average Mach field at the trailing edge for each case, as well as the instantaneous field for the RDC-inlet LES. The RANS simulation predicts a larger suction-side

TABLE IV. Overall supersonic turbine performance comparison between three cases: the RANS simulation, the steady-inlet LES, and the RDC-inlet LES.

Parameter	RANS	LES steady-inlet	LES RDC-inlet
Efficiency (%)	63.6	75.3	68.8
Work (kJ kg^{-1})	413	490	484
Entropy (J kg^{-1} K^{-1})	112.8	84.4	104.7
Flow turning (°)	39.9	43.8	43.3

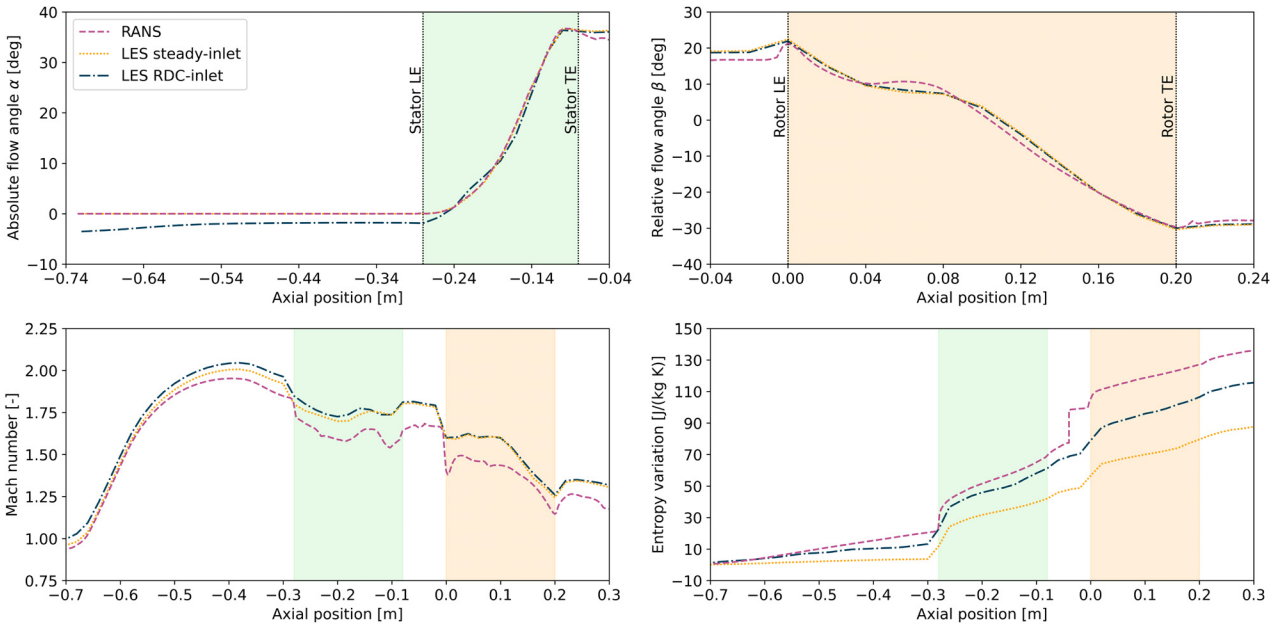

FIG. 5. Comparison of the time- and mass-flow-averaged axial trends (flow angles, Mach number, and entropy variation) between the RANS simulation, the steady-inlet LES, and the RDC-inlet LES. The green and orange shaded areas correspond, respectively, to the stator and rotor blade.

flow separation compared to the steady-inlet LES; this is expected since RANS models have a tendency to predict a larger extent of the separation region due to lower turbulence activity in the separated flow.[57] While this larger separation does not directly impact flow angles (which remain consistent up to the trailing edge), it affects the base region, a dead air zone behind the trailing edge where low-momentum and constant-pressure flow recirculates. The pressure in this base region is crucial in determining the strength of the trailing-edge shock, which in turn influences the deviation as the flow passes through.[58] Hence, the under-turning in the RANS simulation occurs as the flow passes through the stronger trailing-edge shock, generated by an incorrect value of the pressure in the base region due to the overprediction of the flow separation on the suction side [Fig. 6(a)].

In contrast, the steady-inlet LES shows that while separation initiates in a similar position, the flow reattaches before the trailing edge, resulting in a reduced trailing-edge wave angle and limited deviation

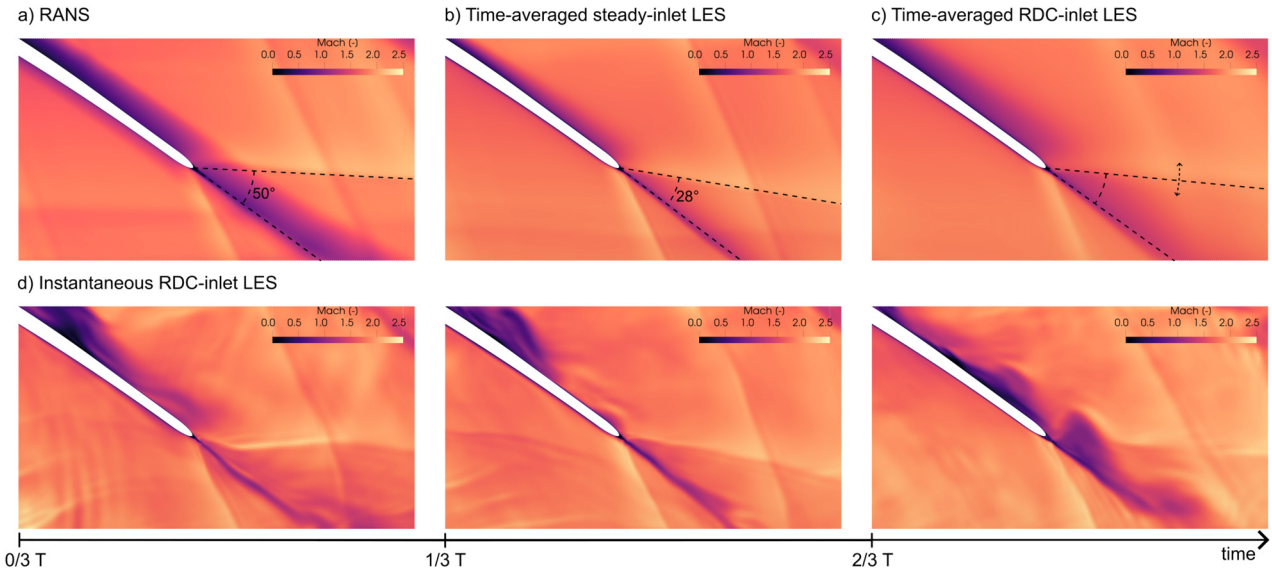

FIG. 6. Comparison of the Mach field at the trailing edge between the RANS simulation (**a**), the time-averaged steady-inlet LES (b), and the time-averaged RDC-inlet LES (c). In (d), three instantaneous snapshots equally spaced in the period T of the detonation wave display the unsteady flow behavior observed in the RDC-inlet LES.

[Fig. 6(b)]. The RDC-inlet LES average field indicates larger suction-side separation, though the exact location of the oblique shock is difficult to discern due to the averaging of this fluctuating feature [Fig. 6(c)]. The instantaneous snapshots provide insight into the flow behavior at the trailing edge, showing large separation pockets on the suction side interspersed with regions of attached flow. This intermittent pattern drives fluctuations in the trailing-edge shock. However, the shock motion remains limited because the conditions at the trailing edge fluctuate so rapidly (high reduced frequency). This phenomenon accounts for the limited flow deviation in the RDC-inlet LES despite the presence of substantial separation pockets. Further insights on shock wave dynamics across a range of reduced frequencies are available in Ref. 21.

In the RDC-inlet LES, the inlet flow angle is non-zero due to the rotation induced by the oblique shock present in the detonation wave structure. A key advantage of the supersonic transition duct is its ability to mitigate flow angle fluctuations by significantly increasing the axial velocity component. This effect is illustrated in the axial trend of the flow angle, which decreases from an average of –3.5° to –1.8° along the duct (Fig. 5). Furthermore, flow angle fluctuations at mid-height are significantly reduced, with the range narrowing from –25° to 13° at the inlet to just –8° to 3° at the outlet. This substantial reduction in flow angle variation enhances the performance of the supersonic inlet turbine, which suffers in off-design angle conditions.[18]

In the transition duct, the Mach number in the RDC-inlet LES is slightly higher than in the steady-inlet LES due to tangential and radial velocity components introduced by the RDC flow. However, these non-axial components dissipate in the stator blade row, resulting in nearly identical axial Mach number trends in the rotor for both LES cases. On the contrary, the Mach number at the outlet of the duct in the RANS simulation is lower than in the steady-inlet LES, and this difference propagates throughout the length of the machine.

The observed Mach number difference can be traced to the behavior of the boundary layer (Fig. 7). In the RANS simulation, the end wall boundary layer is turbulent from the start, as no transition model is applied. Conversely, in the steady-inlet LES, the inlet flow is laminar and remains so until reaching the blade channel. This results in a thinner boundary layer in the steady-inlet LES, increasing the effective area variation in the duct and subsequently raising the Mach number. In the RDC-inlet LES, the boundary layer includes a logarithmic region, but the transition to turbulent conditions occurs at a larger distance from the wall.

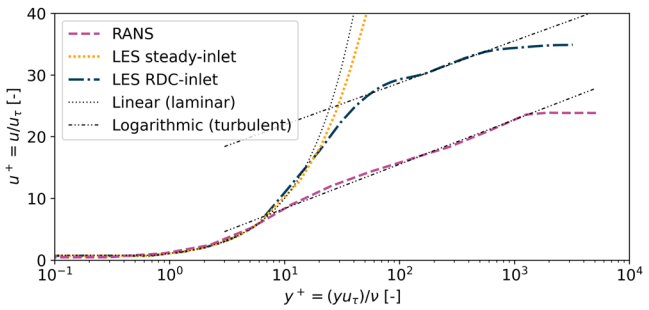

FIG. 7. Mean velocity profiles at the hub wall, extracted at one-fifth of the chord length upstream of the stator leading edge. CFD simulation results are compared with theoretical profiles.

The delayed transition with the increased size of the viscous laminar sublayer can be attributed to the large flow acceleration within the supersonic duct. Sandberg and Michelassi[59] introduced a coefficient K [Eq. (1)] to assess the intensity of flow acceleration for compressible flows; if K exceeds $3.5 \cdot 10^{-6}$, the boundary layer is likely to relaminarize due to strong acceleration. In the supersonic transition duct, the maximum acceleration is registered immediately after the throat with a peak K value of 3.1×10^{-6}. The proximity to the threshold value explains the delayed transition observed in the RDC-inlet LES. Then, as the flow encounters the bow shock waves generated by the stator leading edge, the boundary layer becomes fully turbulent, even in the steady-inlet LES,

$$K = \frac{1}{Re}\frac{1}{M_{is}^2}\left(1+\frac{\gamma-1}{2}M_{is}^2\right)\underbrace{\frac{d}{ds}\left(\frac{M_{is}}{\sqrt{1+\frac{\gamma-1}{2}M_{is}^2}}\right)}_{acceleration}. \quad (1)$$

The primary source of loss generation in the transition duct is viscous entropy production at the wall, meaning that variations in boundary layer characteristics directly impact loss values in this section. Specifically, the thin laminar boundary layer in the steady-inlet LES produces fewer losses compared to the fully turbulent boundary layer in the RANS simulation. Entropy production trends in the stator and rotor are consistent across all three cases (the local entropy jump in the RANS is caused by the mixing plane interface). A detailed discussion about the loss mechanisms in a supersonic inlet turbine is provided in Sec. IV.

Finally, the comparison across the three cases is completed by examining the blade-to-blade and axial planes. As the supersonic flow encounters the blades, bow shock waves are generated from the leading edge, and they are reflected several times in the blade channel (Fig. 8). As previously discussed, flow separation and the downstream wake are more pronounced in the RANS simulation compared to the LES cases (marked as circle A in Fig. 8). In the RANS simulation, the lower Mach number at the inlet of the rotor modifies the position of the intersection point of the two bow-shock waves and their asymptotic slope (circle B in Fig. 8). This variation has two relevant effects: RANS simulations offer a more conservative prediction of collective shock unstarting[16] (the intersection between the bow shock waves moves upstream) and the position of the shock reflection points changes significantly. The second effect is especially clear when comparing the RANS simulation with the steady-inlet LES. In the RANS case, the oblique shock impinges on the rotor suction side at a favorable position with a limited adverse pressure gradient (circle C in Fig. 8). In contrast, the lower asymptotic angle of the bow shock in the steady-inlet LES shifts the reflection point into a region with a stronger pressure gradient, resulting in the formation of a larger separation bubble.

In the RDC-inlet LES, the average flow field shares similarities with the steady-inlet LES [Fig. 8(c)], though many flow details are obscured by time-averaging. The instantaneous flow behavior in an RDE-driven supersonic turbine is shown in Fig. 8(d), where the RDC wave's passage creates a sharp increase in total pressure and inlet Mach number within the blade channel. This sudden rise in mass flow and loading strains the blade's flow-turning capability, causing flow separation along the suction side. As the wave moves downstream, the separated flow is expelled into the wake, allowing the stator suction side to return to its usual conditions. On the rotor, flow separation also occurs periodically, triggered by high relative Mach numbers that produce shock waves reflecting into areas with adverse pressure gradients.

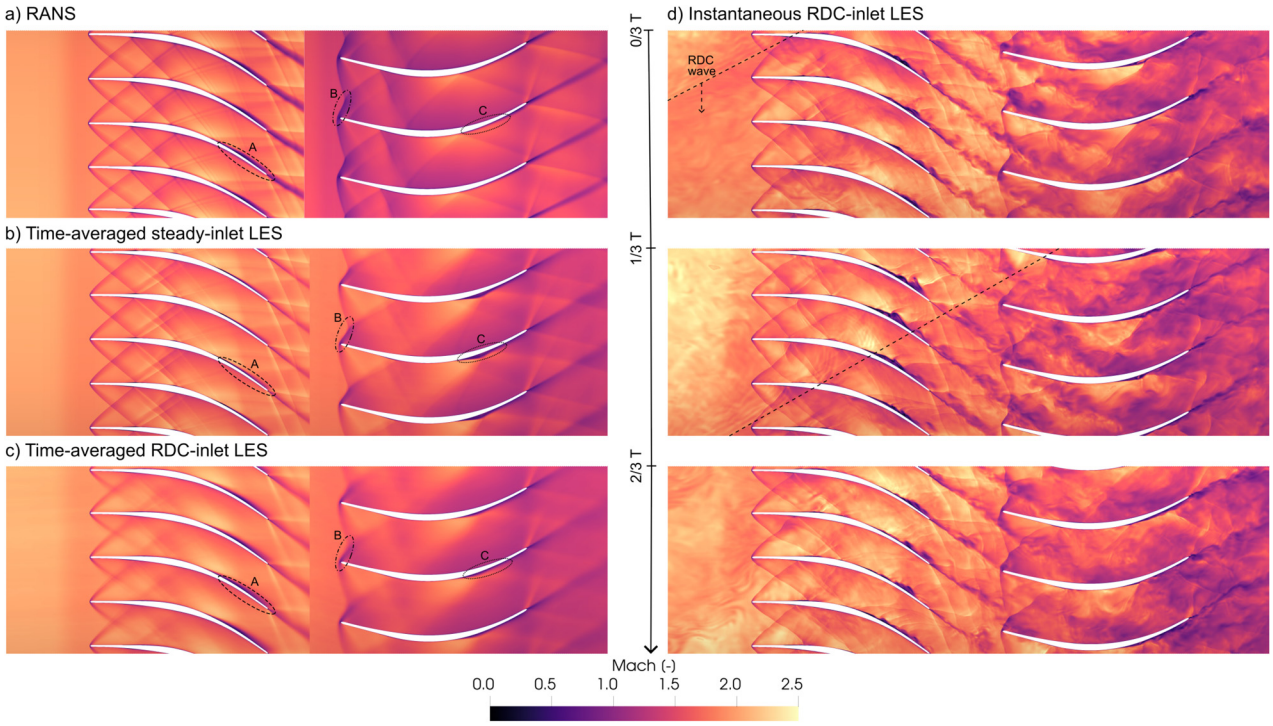

FIG. 8. Comparison of the Mach field in the mid-height blade-to-blade plane between the RANS simulation (a), the time-averaged steady-inlet LES (b), and the time-averaged RDC-inlet LES (**c**). In (d), three instantaneous snapshots equally spaced in the period T of the detonation wave display the unsteady flow behavior observed in the RDC-inlet LES.

At the stator outlet, two primary loss-generation cores (circles I and II in Fig. 9) are visible across all simulations, including RANS; however, the wake in the RANS simulation is substantially larger than in both LES cases. This larger wake, combined with the end wall boundary layer, reduces the effective flow area and accounts for the lower Mach number observed at the stator outlet in RANS. In the RDC-inlet LES, the flow alternates between large and small separations along the suction side, resulting in a wake size between the extensive separation seen in RANS and the reduced separation of the steady-inlet LES. Interestingly, the RDC-inlet LES and the RANS simulation show closer agreement in end wall boundary layer thickness and the interaction between blade wake and end walls (circles III). Furthermore, the RDC-inlet LES exhibits lower total pressure in the core flow due to the mixing of highly non-uniform and unsteady inlet conditions.

While significant differences were observed at the stator outlet across the three cases, the flow fields at the rotor outlet are notably similar (Fig. 10). This observation will be consistent even in the analyses presented in Sec. IV and underlines stator's critical role in moderating even the highly variable conditions introduced by the RDC. By filtering these extreme inlet conditions, the stator enables the rotor to maintain a stable performance. A minor separation zone is observed on the suction side near the hub wall, but the flow remains attached along the trailing edge across most of the blade height. Additionally, one branch of the fishtail shock is visible as a jump in total pressure (dashed red line).

IV. AERODYNAMIC LOSSES

Understanding and quantifying losses is essential for refining the aerodynamic design of turbines, especially when developing novel machines for unconventional applications. This section first presents overall loss production values, followed by a detailed loss analysis to identify the underlying physical mechanisms and regions with the highest entropy generation.

Table V summarizes the total entropy production in both stator and rotor blades across the three simulations and the loss models commonly implemented in mean-line design codes. Entropy variation is commonly calculated using mass-flow-averaged quantities upstream and downstream of each blade row. The steady-inlet LES shows the lowest entropy production in the stator, followed by the RDC-inlet LES and then the RANS simulation. The increased entropy in the RDC-inlet LES, compared to the steady-inlet LES, is due to the mixing of highly non-uniform and unsteady inlet flow conditions. The RANS simulation exhibits the highest entropy production in the stator due to extensive flow separation on the suction side.

In the rotor, this order reverses with the RANS simulation showing the lowest entropy generation. This occurs because the mixing-plane interface in the RANS setup removes the tangential non-uniformities before they reach the rotor. Conversely, in both LES cases, stator wakes and flow non-uniformities are carried into the rotor and dissipated there. Additionally, in the RDC-inlet LES, the rotor continues to dissipate the residual unsteadiness introduced by the inlet flow.

The authors argue that using mass-flow-averaged entropy production data can be misleading, as it attributes losses from the non-uniform inlet conditions to the turbine but disregards the non-uniformities generated by the blade rows themselves. As a result, this approach can falsely suggest a significant drop in turbine performance

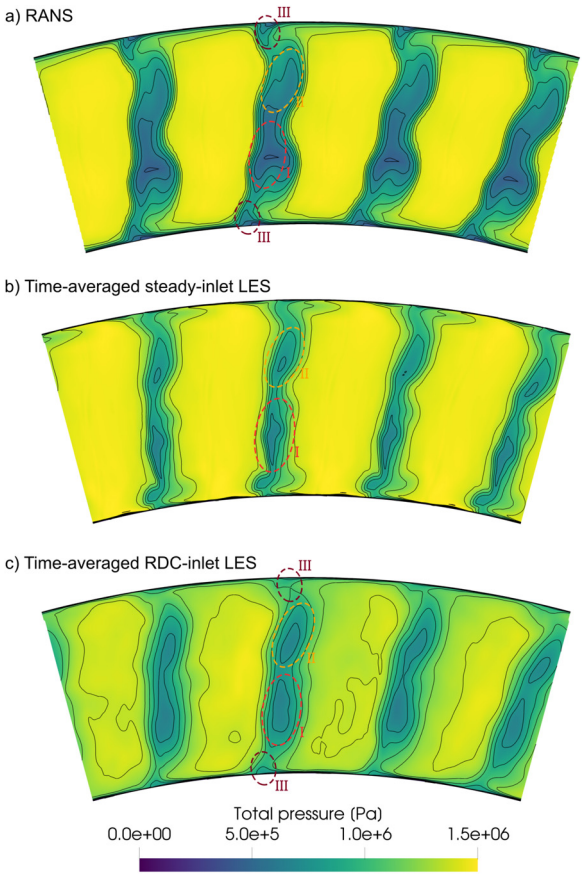

FIG. 9. Comparison of the total pressure field on an axial plane located 1/5 of chord downstream of the stator trailing edge. (**a**), (**b**), and (**c**) display, respectively, the flow field of the RANS simulation, the time-averaged steady-inlet LES, and the time-averaged RDC-inlet LES.

under RDC flow conditions. To better isolate turbine losses from those due to inlet mixing, the entropy increase for each blade row was determined as the difference between the mixed-out outlet and inlet states. A mixed-out state represents a condition of complete mechanical and thermal equilibrium derived from the initial non-uniform flow field

TABLE V. Entropy production (Δs) in the stator and rotor calculated using both mass-flow-averaged and mixed-out quantities. Four cases are compared: RANS simulation, steady-inlet LES, RDC-inlet LES, and the loss models commonly implemented in mean-line design codes.

Component	Case	Mass-averaged [J/(kg K)]	Mixed-out [J/(kg·K)]
Stator	RANS	61.0	74.4
	LES steady-inlet	44.4	53.3
	LES RDC-inlet	58.0	52.5
	Loss models	···	59.8
Rotor	RANS	37.6	37.7
	LES steady-inlet	40.0	36.3
	LES RDC-inlet	47.0	37.1
	Loss models	···	31.8

while conserving mass flow rate, axial momentum, angular momentum, and energy. For a detailed description of the analytical procedure to calculate mixed-out states in turbomachinery flows, refer to Prasad.[56] Unlike mass-flow-averaged quantities, which vary with the reference plane position, the mixed-out state remains axially invariant and accumulates all the losses that can be inferred from the initial state. In the stator, the RANS simulation shows the highest mixed-out entropy increase due to the large wake area at the stator outlet (Fig. 9). By contrast, the stator entropy change for the two LES simulations is nearly identical. In the rotor, mixed-out entropy values are close across all three cases, consistent with similar flow fields observed in the rotor (Sec. III). Additionally, the turbine's total-to-total efficiency calculated from mixed-out states is 73.7% in the steady-inlet LES and 73.0% in the RDC-inlet LES. These findings highlight that the turbine design methodologies are effective, as performance is minimally impacted by the extreme RDC inlet flow conditions.

Since the initial design of a supersonic inlet turbine typically relies on a mean-line code, evaluating the performance of standard loss models in this context is valuable. The mean-line code generally includes the following primary sources of loss generation:

1. Leading-edge bow shock wave: predicted with Moeckel's theory[60] and corrected for the asymptotic slope.[16]
2. First oblique shock reflection: calculated with the classic theory of aerodynamics.[61]

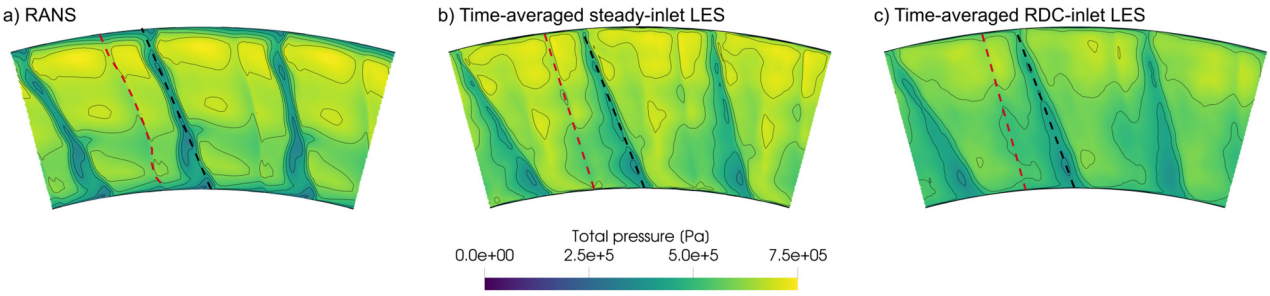

FIG. 10. Comparison of the total pressure field on an axial plane located 1/5 of chord downstream of the rotor trailing edge. (a)–(c) display, respectively, the flow field of the RANS simulation, the time-averaged steady-inlet LES, and the time-averaged RDC-inlet LES. The black dashed line is the location of rotor trailing edge, while the red dashed line is a branch of the fishtail shock.

3. Boundary and mixing losses: assessed with Stewart's methodology.[62]
4. End wall losses: determined by integrating Coull's loss model[63] with the flow field estimated from the profile method of characteristics.

For further details on these loss models and their integration into mean-line codes for supersonic inlet turbines, refer to the works of Mushtaq *et al.*[7,18] The losses predicted by these models are compared against the mixed-out entropy increase because Stewart also assumes a mixed-out state to calculate the wake mixing losses. Compared to LES results, the loss models tend to overestimate stator losses while underestimating rotor losses, with the two discrepancies counterbalancing each other. In the RANS simulation, stator entropy increase significantly exceeds predictions from the loss models, which is expected given that the extensive flow separation on the suction side is not captured in these models.

Zhao and Sandberg[26] recently proposed an entropy decomposition framework that enables the identification of distinct physical mechanisms contributing to loss generation within each cell of the computational domain. In a blade row, entropy production is caused by mean viscous dissipation V_M, mean flow irreversible heat flux H_M, turbulence production related to Reynolds stresses P_R, turbulent heat flux H_R, and advection of the turbulent kinetic energy A_k as follows:

$$\tilde{G}_s = \underbrace{\frac{1}{\tilde{T}}\sigma_{ij}(\tilde{u})\frac{\partial \tilde{u}_j}{\partial x_i}}_{V_M} + \underbrace{\frac{c_p\mu}{\mathrm{Pr}}\frac{1}{\tilde{T}^2}\left(\frac{\partial \tilde{T}}{\partial x_i}\right)^2}_{H_M} + \underbrace{\frac{1}{\tilde{T}}\tau_{ij}^R\frac{\partial \tilde{u}_j}{\partial x_i}}_{P_R} \underbrace{-\frac{1}{\tilde{T}}\frac{\partial}{\partial x_i}\left(q_i^R\right)}_{H_R} \underbrace{-\frac{1}{\tilde{T}}\frac{\partial(\bar{\rho}\tilde{u}_i k)}{\partial x_i}}_{A_k} \quad (2)$$

Each of these entropy production terms was computed for a stream tube located around the blade mid-height, and the total entropy generation for both steady-inlet and RDC-inlet LES is shown in Fig. 11. In the steady-inlet LES, the areas of highest entropy generation in the stator and rotor include the leading-edge bow shock waves, the first oblique shock reflection, suction-side flow separation, the blade profile, the wake, and the fishtail shock waves. A large concentration of losses is located around the rotor bow shock due to its interaction with the stator wake, resulting in a combination of shock and wake losses in these cells. Regions of negative entropy appear behind the shocks and in separated flows, a result of turbulent heat transfer (H_R) from hotter to cooler areas; however, this effect does not occur at the stator bow shock, as the flow is still laminar at the blade row inlet in the steady-inlet LES. In the RDC-inlet LES, the regions of the highest entropy production are similar to those observed in the steady-inlet LES. However, a key difference is the increased entropy generation in the core flow, which results from the turbulent mixing of the highly unsteady and non-uniform inlet conditions. Additionally, in the stator blade channel, a larger area is impacted by shock losses due to their fluctuations in space and time.

The entropy generation flow field confirms that the primary sources of loss have been accounted for in the mean-line design approach. However, it is recommended that designers incorporate an additional loss model to account for fishtail shock waves, as their contribution to overall entropy generation should not be overlooked.

Once the entropy generation terms have been calculated in each cell, it is possible to perform a volume integral on the entire stream tube to quantitatively establish the weight of each loss mechanism (Fig. 12); for the comparisons, the integral values are normalized by the number of simulated blade channels. For the sake of brevity, the discussion here will be limited to the stator, because this component is the most affected by the RDC-inlet conditions. With more than 70% of entropy generation, turbulent loss mechanisms (P_R, H_R, and A_k) are dominant with respect to mean flow contributions (V_M and H_M), and this difference is even more pronounced in the RDC-inlet LES. In traditional systems, turbulent loss mechanisms contribute to 45% of the entropy generation in the stator of a high-pressure turbine[26] and 65% in the rotor of a transonic compressor.[64] Entropy generation due to turbulent production P_R is markedly high because turbulent kinetic

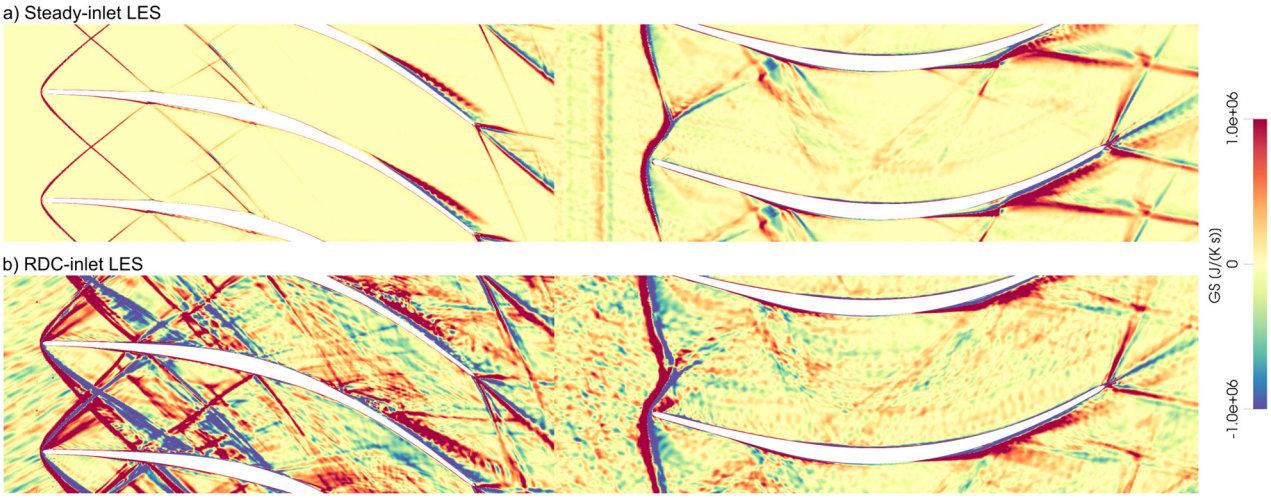

FIG. 11. Total entropy generation $\tilde{G}_s$ [as defined in Eq. (2)] at the mid-span blade-to-blade plane of the supersonic inlet turbine for the steady-inlet LES (a) and the RDC-inlet LES (b).

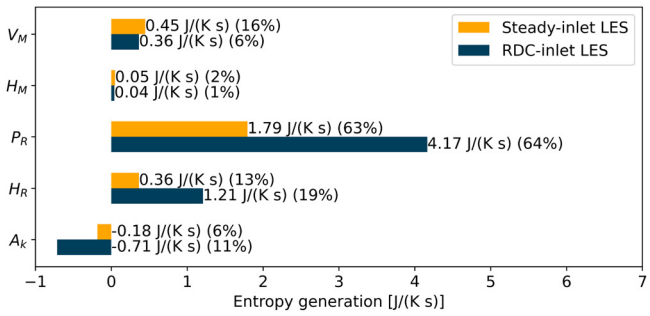

FIG. 12. Entropy generation breakdown by physical mechanisms following Zhao and Sandberg's framework,[26] with a comparative analysis between the steady-inlet LES and the RDC-inlet LES results.

energy is amplified with each shock passage.[65] Additionally, as highlighted by Zhao and Sandberg,[26] the advection term A_k can become negative in LES simulations, indicating an inverse energy cascade in which turbulent kinetic energy reconverts into mean kinetic energy.

To further assess entropy generation, the computational domain was segmented into four regions: shocks, profiles, wakes, and the core flow [Fig. 13(a)]. This breakdown provides insights that are intuitive for turbomachinery designers and aligns with traditional loss correlations. Classification criteria were applied to assign each computational cell to the appropriate region. Pressure gradients, rather than density gradients, were used to identify shocks without including the boundary layers, which belong to the profile loss region. The profile loss region was defined by offsetting the blade profile in the normal direction, while the wake region extends downstream from the profile following the geometric angle with a spread angle of 3°. Cells that overlapped between the shock, profile, and wake loss regions were exclusively assigned to the wake loss region. Similarly, cells that were part of both the profile and shock loss regions were assigned solely to the shock region. All other cells were designated as core flow (checks ensured that each cell was uniquely assigned to a single region).

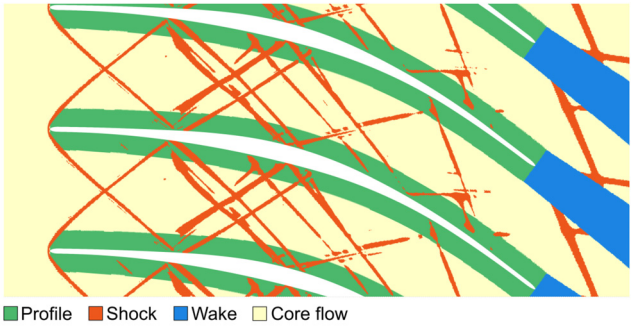

(a)

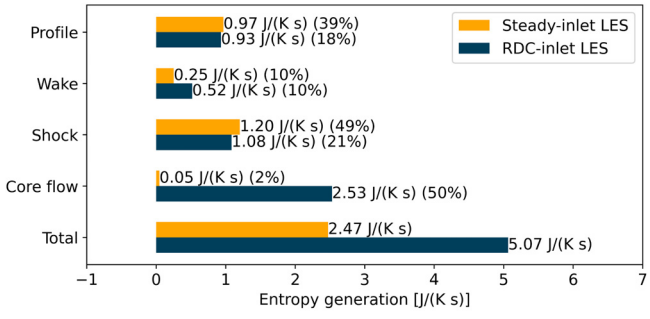

(b)

FIG. 13. (a) Segmentation of the domain into four regions for the steady-inlet LES: profile, shocks, wake, and core flow. (b) Comparison of total entropy generation across each region within the mid-span stream tube for both steady-inlet LES and RDC-inlet LES cases.

In the steady-inlet LES, shock losses are the largest source of entropy generation, contributing 49% of the total, followed by profile losses at 39% and wake losses at 10% [Fig. 13(b)]. In the RDC-inlet LES, these values largely remain the same, but core flow losses show a marked increase, exceeding double the shock-related losses. This rise in core flow losses is linked to the mixing of the highly non-uniform flow from the combustor, which also drives the increase in turbulent fluctuation losses. This analysis confirms that, when mixing losses from non-uniform inlet conditions are excluded (through entropy mixed-out analysis), the impact of inlet conditions on supersonic turbine losses is limited. It is relevant to emphasize that this observation applies within the context of the design methodologies outlined in Sec. II A.

V. UNSTEADY FLOW INTERACTIONS

This section examines the impact of RDC-inlet conditions on the unsteady flow dynamics within the supersonic turbine. Specifically, it delves into two key phenomena: the interaction and propagation of the RDC wave through the stator and rotor blade rows, and the flow separation occurring along the suction side of the stator.

A. RDC wave propagation in a supersonic inlet turbine

To analyze the propagation of the RDC wave within the supersonic turbine, it is essential to isolate its effects from other unsteady flow components. The phase-locked average (PLA) technique is used for this purpose, whereby a time signal is divided into periods based on a specific phase reference, typically the periodic passage of a blade.[66] An ensemble average is then conducted across all instances with the same phase value. PLA is particularly beneficial because it preserves both the time-averaged value and the deterministic components associated with the targeted phenomenon while filtering out the deterministic and stochastic components from unrelated phenomena. Given these characteristics, a PLA with the RDC wave passage as the phase reference is well-suited for investigating the influence of RDC-inlet conditions within the supersonic turbine.

The results of the PLA are presented through phase–phase diagrams,[67] where the horizontal axis represents the relative phase with respect to the moving RDC wave, and the vertical axis indicates the relative phase with respect to the stator vane (Fig. 14). Phase–phase diagrams were chosen instead of phase-time diagrams to distinguish the contributions from each component clearly: the RDC wave, stator, and rotor features appear along vertical, horizontal, and diagonal lines, respectively. Each diagram corresponds to a specific radial height; however, since the main effects of the RDC-inlet conditions are clearly observed at mid-height and radial effects are not essential to this

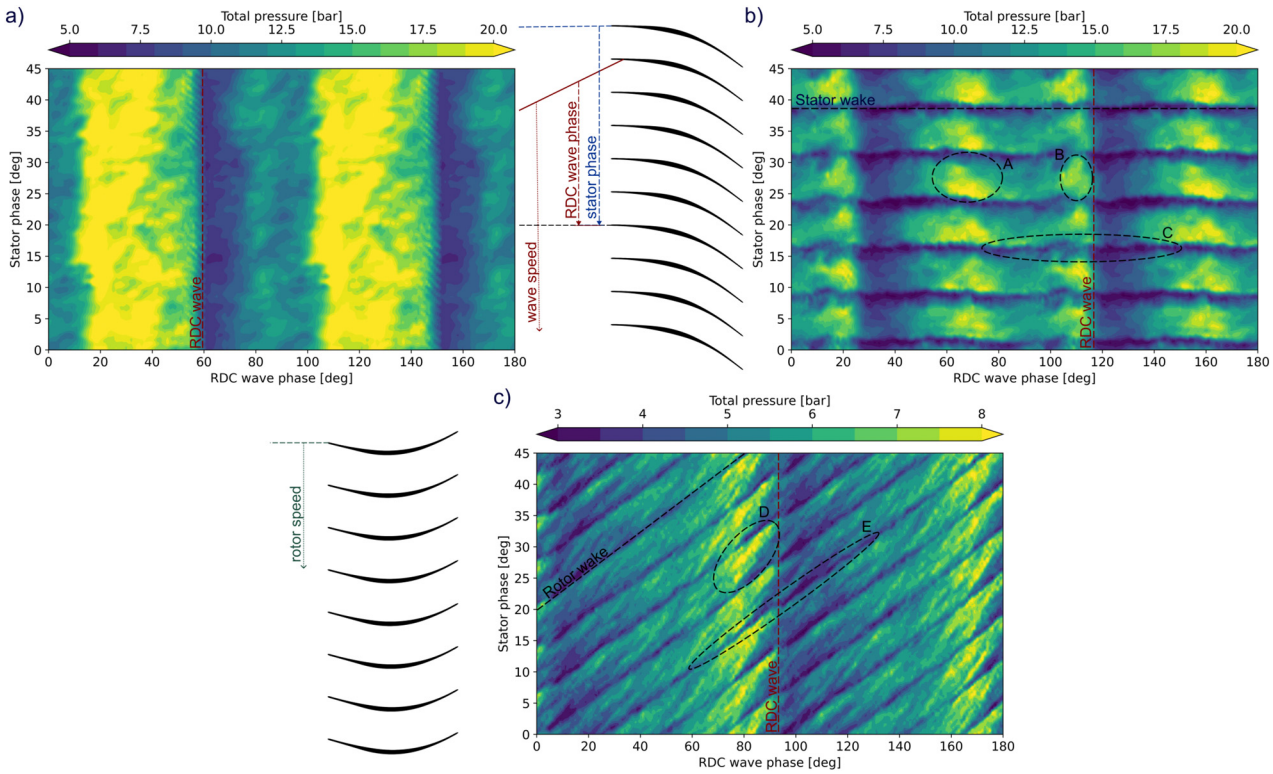

FIG. 14. Phase–phase diagrams of the phase-locked average total pressure at three locations: (a) stator inlet, (b) stator outlet, and (c) rotor outlet. Total pressure data are extracted at mid-height on axial planes positioned at one-fifth of the chord length upstream or downstream of the stator or rotor blade.

discussion, only the mid-height phase–phase diagrams are presented here for the sake of brevity.

Figure 14(a) shows the total pressure phase–phase diagram at the stator inlet. The flow field exhibits a repeating pattern every 90° on the x-axis due to the four detonation waves rotating within the combustion chamber. Interestingly, the increase in total pressure caused by each detonation wave is not confined to a narrow region near the wave itself as at the inlet of the transition duct (Fig. 1). Instead, the period can be divided into two distinct phases of nearly equal duration: one characterized by high total pressure and the other by low total pressure. As a result, the stator blades experience alternating conditions, with high total pressure for half of the time and low total pressure for the other half.

At the outlet of the stator [Fig. 14(b)], the high total pressure region expands further, covering nearly 70° of the RDC wave period. Within this extended high-pressure area, two distinct high-pressure cores are evident. The first core appears, marked with the circle B in Fig. 14(b), directly behind the RDC wave and exhibits a nearly uniform distribution across the pitch. The second core [area A in Fig. 14(b)] is located toward the trailing side of the high total pressure region and it is concentrated along the pressure side of the blade. This asymmetry results from the inclination of the RDC wave, which directs high total pressure flow onto the blade's pressure side, leading to a total pressure buildup in this region. The flow pattern produced by the stator repeats every 7.5° vertically, which is consistent with the number of stator blades. The phase–phase diagram further highlights the impact of the RDC wave on the stator wake [area C in Fig. 14(b)]. As discussed in Sec. III, the maximum flow separation occurs each cycle as the high total pressure wave enters the stator blade row. However, as the RDC wave exits the stator, the separated flow is also discharged downstream. This phenomenon initially amplifies the wake width, which is then reduced to its smallest size after the passage of the RDC wave.

In the rotor's relative frame of reference, the RDC wave's apparent rotational speed decreases because both the wave and the rotor move in the same direction. Consequently, the RDC wave takes longer to complete a full cycle, resulting in a lower reduced frequency seen by the rotor. Future investigations could explore how the performance of the supersonic inlet turbine might vary if the rotational direction of the rotor was reversed relative to the RDC wave. In this specific configuration, the rotational direction of the rotor was chosen to ensure that the RDC oblique shock wave impacts the stator's pressure side rather than the suction side, which is already prone to flow separation issues.

In the phase–phase diagram, rotor wakes and other rotor-related features appear along the diagonal direction [Fig. 14(c)]. Although the first stage significantly attenuates the RDC-inlet conditions, the total pressure front generated by the RDC wave is still visible at the rotor outlet, suggesting that subsequent stages might experience some residual effects. Additionally, this high total pressure front appears slightly tilted within each rotor pitch [area D in Fig. 14(c)]. This tilt occurs because the high-pressure flow exiting the stator initially impacts the rotor's pressure side, causing the high total pressure conditions to reach the rotor outlet on the pressure side before extending to the

suction side. The rotor wake behavior [area E in Fig. 14(c)] is less influenced by the RDC wave, as there is no flow separation at the trailing edge (Fig. 8).

In conclusion, the unsteadiness generated by the RDC within the turbine can be quantified by examining the standard deviation of total pressure across the RDC wave phase. Starting from a standard deviation of 4.3 bar at the stator inlet, this value decreases to 2.3 bar at the stator outlet and further to 0.7 bar at the rotor outlet. Hence, the supersonic inlet turbine effectively attenuates the intensity of RDC-generated fluctuations by 84%.

B. Reduced order modeling of the suction side flow separation

The flow separation on the suction side of the stator blade differs significantly between the steady-inlet and RDC-inlet large-eddy simulations. While Lui *et al.*[25] have previously analyzed flow behavior under steady-inlet conditions, no prior studies have investigated how RDC-inlet conditions influence the unsteady dynamics of flow separation on the suction side. To address this, two complementary methods are applied: dynamic mode decomposition (DMD) to identify dominant modes associated with flow separation, and a shallow recurrent decoder (SHRED) architecture to develop an efficient and accurate reduced-order model.

The initial step for both methodologies is to confine the analysis to a narrow window surrounding the separated flow on the suction side. This operation reduces the computational time and enhances the convergence of the data analysis algorithms.

Dynamic mode decomposition (DMD) is a data-driven algorithm that decomposes data into a series of dynamic modes, ϕ_j, each with an associated eigenvalue ω_j and loading b_j [Eq. (3)].[27] A key feature of DMD, which makes it particularly suitable for this analysis, is its capacity to reveal spatiotemporal coherent structures within high-dimensional time-series data. This is possible since this technique combines the strengths of the proper orthogonal decomposition in space with the Fourier transform in time.[27] Since Schmid's original algorithm,[68] various DMD versions have been developed. For this study, the bagging optimized dynamic mode decomposition (BOP-DMD)[69] is selected due to its robustness against noise and its ability to generate uncertainty quantification metrics.

$$x(t) = \sum_{j=1}^{r} \varphi_j e^{\omega_j t} b_j = \Phi \exp(\Omega t) \mathrm{B}. \tag{3}$$

To understand and isolate the impact of the RDC on flow separation, DMD is applied to phase-locked-averaged quantities with their mean values subtracted. A six-frequency mode decomposition (corresponding to a subspace rank of 12, with complex conjugate eigenvalue pairs constrained to be imaginary due to the periodic nature of the flow) proves sufficient to capture the dynamics of the PLA flow field accurately. Figure 15 displays the dynamic modes 1–3 of the total pressure and modes 4–6 of the tangential component of the velocity, with tangential defined relative to the turbine's reference frame (the remaining modes are omitted for the sake of brevity, as they do not provide essential information). The DMD analysis identifies frequencies that are multiples of the detonation wave frequency. While this is expected given the PLA preprocessing, it is noteworthy that these dominant RDC-related frequencies persist even when the DMD is applied to the raw flow quantities without prior PLA preprocessing.

In the dynamic modes of total pressure, the detachment of the high-pressure strip indicates the onset of flow separation near the wall (ellipse A in Fig. 15). The first two dynamic modes (area B in Fig. 15) represent the passage of the two high-pressure cores [area A and B in Fig. 14(b)]. In the first mode, the high-pressure region located farther

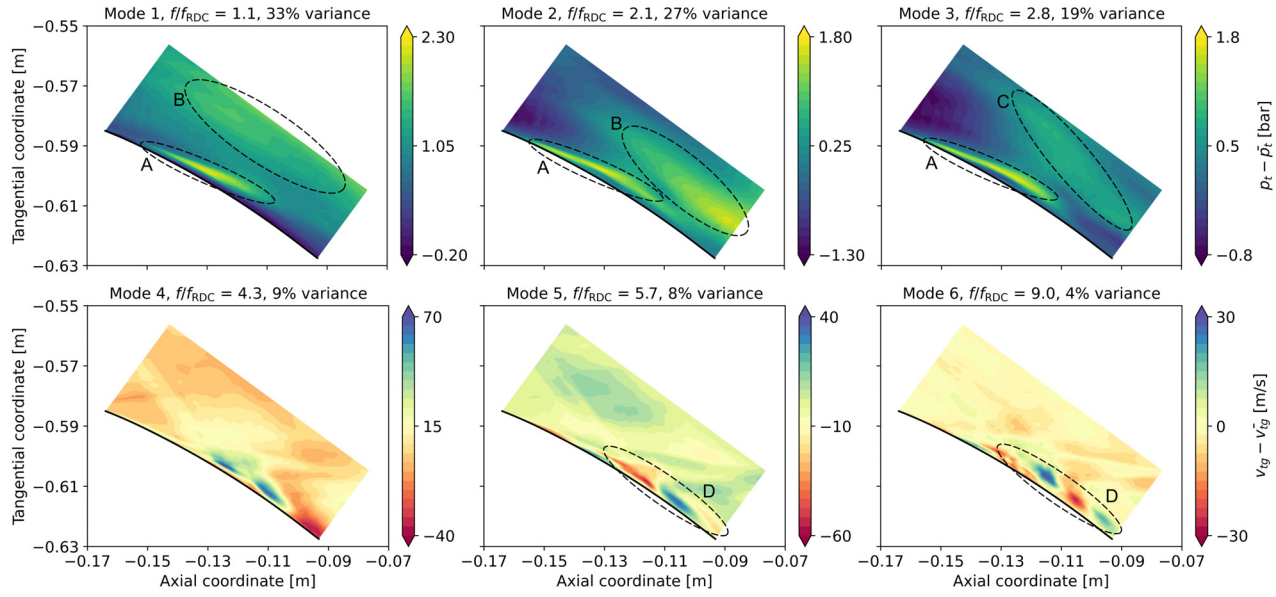

FIG. 15. Dynamic mode decomposition of the PLA total pressure and tangential velocity components within a window surrounding the separated flow on the stator blade's suction side. Modes 1–3 correspond to the total pressure decomposition, while modes 4–6 represent the tangential velocity component decomposition.

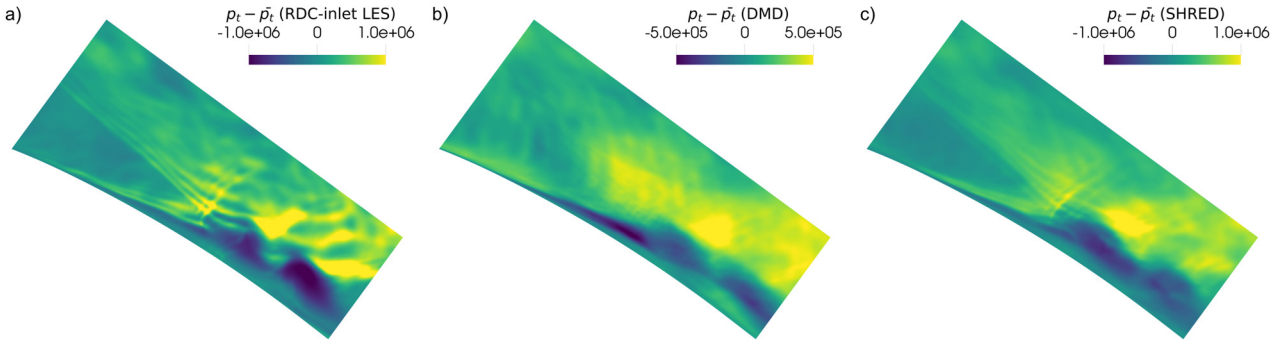

FIG. 16. Comparison of total pressure fields: (a) a snapshot from the RDC-inlet LES, (b) the reconstructed field using DMD, and (c) the reconstructed field using SHRED.

from the suction side corresponds to the accumulation of total pressure on the blade's pressure side. The second mode reflects a frequency that allows the formation of two high-pressure cores within each detonation wave cycle. The third mode captures the reflection of the high-pressure wave on the pressure side of the blade wall (area C in Fig. 15). This mode is particularly significant, as the reflected wave periodically interacts with the suction side, actively ejecting the separated flow and influencing its unsteady dynamics.

The high-frequency modes of the tangential velocity component reveal the shedding and convection of Kelvin–Helmholtz vortical structures[25] (ellipse D in Fig. 14), which are characteristic of the flow separation on the suction side. These vortical structures arise from the combined effects of the oblique shock wave reflecting on the suction side of the blade (Fig. 8) and the abrupt increase in mass flow and loading induced by the passage of the RDC wave. In addition, the movement of the oblique shock is influenced by fluctuations in the Mach number, highlighting a strong coupling between the flow separation dynamics and the unsteady flow delivered by the RDC.

Furthermore, the first three modes collectively capture nearly 80% of the variance in the flow field, indicating that the alternating high and low total pressure conditions generated by the RDC are the primary source of unsteadiness. However, the contribution of vortex shedding is also significant, representing the remaining 20% of the unsteadiness. This analysis yields a key insight: while the mean flow field and loss characteristics show limited differences between the steady-inlet and RDC-inlet LES, capturing the unsteady flow features unique to supersonic turbines operating with RDEs requires inlet conditions representative of the RDC.

To further refine the analysis and develop a reduced-order model of the flow separation on the suction side, DMD was applied directly to the total pressure data without PLA. Even though the flow field is decomposed with 72 modes, the results reveal significant limitations. While the reconstructed DMD field preserves the broad structure of the high- and low-pressure cores, it fails to capture finer, localized features such as pressure waves. Moreover, the intensity of key flow phenomena is noticeably dampened [Fig. 16(b) with respect to Fig. 16(a)]. These shortcomings are also evident in the area-averaged total pressure over time (Fig. 17): even though the reconstructed DMD field broadly tracks the original trend from the RDC-inlet LES, the maximum and minimum values are notably diminished.

Shallow recurrent decoder (SHRED) neural networks, proposed by Williams *et al.*,[28] have shown exceptional capabilities in both reconstruction and forecasting. This architecture leverages a recurrent neural network (RNN) to capture a latent representation of the temporal dynamics from sensor data, while a shallow decoder maps this latent representation back to the high-dimensional state space.[28] Once trained, SHRED can reconstruct complex flow fields using only a finite time history from a minimal set of randomly placed sensors. These features make SHRED an ideal choice for developing a reduced-order model of the flow separation occurring on the stator blade's suction side.

Using time-history data from three randomly selected points, a long short-term memory (LSTM) network[70] is trained to construct the latent space. LSTMs, as recommended by Williams, excel at capturing both long- and short-term dependencies, making them ideal for this task. Figure 16(c) shows a snapshot of the total pressure field reconstructed using the trained SHRED model. The results are remarkably accurate: the SHRED not only reconstructs the high- and low-pressure cores but also clearly captures the sequence of pressure waves reflected from the pressure side. This level of detail is reconstructed from the data in only three points. The model's accuracy is further verified by its ability to closely replicate the trends in the area-averaged total pressure, as illustrated in Fig. 17.

SHRED outperforms DMD primarily due to its ability to model nonlinear relationships through the neural network layers, unlike DMD, which assumes linear interactions between modes. This capability is essential for accurately capturing complex nonlinear phenomena in the flow, such as shock waves. Increasing excessively the number of

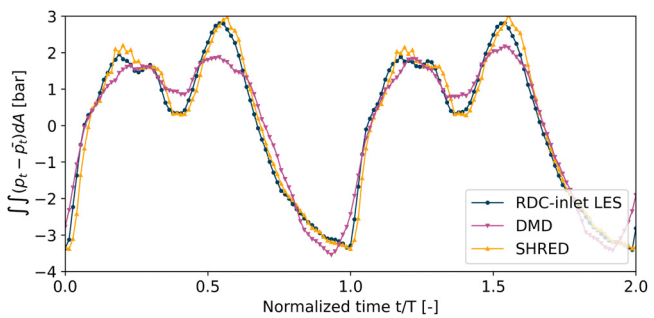

FIG. 17. Time evolution of the area-averaged total pressure within the window surrounding the separated flow on the suction side. The plot compares the original RDC-inlet LES data with the reconstructed data using DMD and SHRED.

modes in DMD to account for localized features often backfires, as it makes the method more noise-sensitive and yields minimal improvement in accuracy. By contrast, SHRED is robust to noise and sensor placement, providing reliable reconstructions without requiring extensive hyperparameter tuning. The remarkable accuracy of SHRED, even under the challenging flow conditions of an RDE, underscores its potential as a valuable tool for modeling, data compression, sensing, and control of advanced systems. However, it is important to acknowledge a key limitation: SHRED's reduced-order model lacks interpretability.

VI. CONCLUSIONS

The integration of a supersonic inlet turbine with a rotating detonation combustor represents a promising engine architecture for both ground power production and aeroengines. This study advances our understanding of this innovative solution by conducting a large eddy simulation of the stator and rotor blade rows of a supersonic inlet turbine operating under RDC-representative inlet conditions.

Serious concerns have emerged from the comparison between the RANS simulation, the steady-inlet LES, and the RDC-inlet LES. The RANS simulation underestimates the flow turning, primarily due to inaccurate pressure values in the base region when moderate flow separation occurs on the suction side. However, a few degrees of error in the flow turning have a huge impact in supersonic inlet turbines, with the RANS underpredicting the total-to-total efficiency by nearly 12%. Furthermore, the Mach number predicted by RANS is lower than that of the LES, a discrepancy attributed to a thicker end wall boundary layer in the RANS results. While significant differences are observed in the stator across the three cases, the impact of the inlet conditions on the rotor flow fields and aerodynamic losses is comparatively modest.

The mixed-out loss analysis revealed that the performance of the turbine is minimally affected by the extreme inlet conditions, demonstrating that the methodologies employed for the turbine design are effective. While mean-line loss models exhibit some inaccuracies, their errors tend to counterbalance, yielding predictions that are acceptable given the complexity of the flow. The entropy decomposition framework revealed that turbulent loss mechanisms produce more than 70% of the entropy in these machines because turbulent kinetic energy is amplified with each shock passage. Additionally, from the entropy generation breakdown into regions, it is also evinced that shock losses are the largest source of loss generation, followed by profile and wake losses.

The phase–phase diagrams vividly illustrate the transformation of high- and low-pressure phases as the RDC wave propagates through the stator and rotor blade rows. At the rotor outlet, while the RDC wave remains detectable, the total pressure fluctuations are attenuated by 84%. This substantial reduction improves the operating conditions for the subsequent turbine stages.

Finally, the interaction between the RDC wave and the flow separation on the stator's suction side was examined in detail. Dynamic mode decomposition highlighted how the unsteady flow features resonate with the RDC-wave frequency. However, DMD faced challenges in accurately reconstructing localized phenomena. In contrast, shallow recurrent decoder neural networks, though lacking interpretability, were successful in delivering an efficient and accurate reduced-order model of the flow separation on the suction side.

This work offered valuable insights into the aerodynamic behavior of a supersonic inlet turbine operating downstream of an RDC. It highlighted the limitations of RANS simulations and clarified which aspects must be prioritized depending on whether the focus is on mean flow behavior or unsteady phenomena. These findings will be essential for further advancing the technology readiness level of RDE systems, paving the way for practical implementation.

ACKNOWLEDGMENTS

This work was conducted as part of the PRIN 2022 project EnaTech-RDE (Id: 2022BW9SHS), funded by the Italian Ministry of University and Research (MUR).

AUTHOR DECLARATIONS

Conflict of Interest

The authors have no conflicts to disclose.

Author Contributions

N. Mushtaq: Conceptualization (lead); Data curation (lead); Formal analysis (lead); Methodology (equal); Project administration (equal); Validation (lead); Visualization (lead); Writing – original draft (lead); Writing – review & editing (equal). **C. P. Arroyo:** Methodology (equal); Software (lead); Visualization (supporting); Writing – review & editing (equal). **J. Dombard:** Methodology (equal); Supervision (equal); Writing – review & editing (equal). **F. Duchaine:** Methodology (equal); Supervision (equal); Writing – review & editing (equal). **P. Strempfl:** Methodology (equal); Writing – review & editing (equal). **P. Gaetani:** Funding acquisition (lead); Methodology (equal); Project administration (equal); Supervision (equal); Writing – review & editing (equal).

DATA AVAILABILITY

The data that support the findings of this study are available from the corresponding author upon reasonable request.

NOMENCLATURE

A_k	Entropy generation by turbulent kinetic energy advection [Eq. (2)] [J s^{-1} K^{-1}]
b_j	DMD loadings (-)
c	Chord (m)
c_p	Specific heat at constant pressure (J kg^{-1} K^{-1})
G_s	Overall entropy generation [Eq. (2)] (J s^{-1} K^{-1})
H	Blade height (m)
H_M	Entropy generation by mean flow heat flux [Eq. (2)] (J s^{-1}K^{-1})
H_R	Entropy generation by turbulent heat flux [Eq. (2)] (J s^{-1}K^{-1})
k	Turbulence kinetic energy (m^2 s^{-2})
K	Coefficient of flow acceleration [Eq. (1)] (-)
M	Mach number (-)
P_R	Entropy generation by turbulence production [Eq. (2)] (J s^{-1}K^{-1})
Pr	Prandtl number (-)

q_i	Heat flux ($J\,m^{-2}s^{-1}$)
Re	Reynolds number (-)
r_i	Internal radius (m)
s	Specific entropy ($J\,kg^{-1}K^{-1}$)
T	Temperature (K)
V_M	Entropy generation by mean viscous dissipation [Eq. (2)] ($J\,s^{-1}K^{-1}$)
α	Absolute flow angle (°)
β	Relative flow angle (°)
γ	Specific heat ratio (-)
μ	Dynamic viscosity (Pa s)
τ_{ij}	Reynolds stress tensor (Pa)
χ	Stage reaction: static rotor enthalpy variation/Euler work (-)
σ_{ij}	Viscous stress tensor (Pa)
ϕ_j	DMD dynamic modes [Eq. (3)] (-)
ω	Rotational speed or eigenvalue ($rad\,s^{-1}$)
$()_1$ $()_2$	Stator inlet and outlet, respectively
$()_3$ $()_4$	Rotor inlet and outlet, respectively
$()_{is}$	Isentropic
$()_{res}$	Resolved
$\overline{()}$	Reynolds-average
$\widetilde{()}$	Favre-average
CFD	Computational fluid dynamics
DMD	Dynamic mode decomposition
LES	Large eddy simulation
MOC	Method of characteristics
PLA	Phase-locked average
RANS	Reynolds-averaged Navier–Stokes
RDC	Rotating detonation combustor
RDE	Rotating detonation engine
ROM	Reduced order model
SHRED	Shallow recurrent decoder
URANS	Unsteady Reynolds-averaged Navier–Stokes

REFERENCES

[1]D. Spencer, *bp Energy Outlook* (British Petroleum, 2024).
[2]J. Sousa, G. Paniagua, and E. Collado Morata, "Thermodynamic analysis of a gas turbine engine with a rotating detonation combustor," Appl. Energy **195**, 247–256 (2017).
[3]E. Wintenberger and J. E. Shepherd, "Thermodynamic cycle analysis for propagating detonations," J. Propul. Power **22**, 694–698 (2006).
[4]V. Anand and E. Gutmark, "Rotating detonation combustors and their similarities to rocket instabilities," Prog. Energy Combust. Sci. **73**, 182–234 (2019).
[5]V. Raman, S. Prakash, and M. Gamba, "Nonidealities in rotating detonation engines," Annu. Rev. Fluid Mech. **55**, 639–674 (2023).
[6]J. Braun, G. Paniagua, and D. Ferguson, "Aero-thermal characterization of accelerating and diffusing passages downstream of rotating detonation combustors," in ASME Turbo Expo: Turbomachinery Technical Conference and Exposition, 2021.
[7]N. Mushtaq, G. Colella, and P. Gaetani, "Design and parametric analysis of a supersonic turbine for rotating detonation engine applications," Int. J. Turbomach. Propul. Power **7**, 1–24 (2022).
[8]Z. Liu, J. Braun, and G. Paniagua, "Thermal power plant upgrade via a rotating detonation combustor and retrofitted turbine with optimized endwalls," Int. J. Mech. Sci. **188**, 105918 (2020).
[9]S. Grasa and G. Paniagua, "Design, multi-point optimization, and analysis of diffusive stator vanes to enable turbine integration into rotating detonation engines," J. Turbomach. **146**, 111002 (2024).
[10]K. Nakata, K. Ishihara, K. Goto, N. Itouyama, H. Watanabe, A. Kawasaki, K. Matsuoka, J. Kasahara, A. Matsuo, I. Funaki, K. Higashino, J. Braun, T. Meyer, and G. Paniagua, "Experimental investigation of inner flow of a throatless diverging rotating detonation engine," Proc. Combust. Inst. **39**, 3073–3082 (2023).
[11]J. Braun, J. Saavedra, and G. Paniagua, "Evaluation of the unsteadiness across nozzles downstream of rotating detonation combustors," in 55th AIAA Aerospace Sciences Meeting, AIAA Paper No. AIAA 2017-1063, 2017.
[12]N. Mushtaq, M. Pini, and P. Gaetani, "Advanced design of a transition duct for supersonic inlet turbines in rotating detonation engines," in ASME Turbo Expo: Turbomachinery Technical Conference and Exposition, 2024.
[13]G. Paniagua, M. C. Iorio, N. Vinha, and J. Sousa, "Design and analysis of pioneering high supersonic axial turbines," Int. J. Mech. Sci. **89**, 65–77 (2014).
[14]A. Kantrowitz and C. D. Donaldson, "Preliminary investigation of supersonic diffusers," Report No. NACA-WR-L-713 (NACA, 1945).
[15]L. B. Inhestern, D. Peitsch, and G. Paniagua, "Reduced-order-modeling of the transient starting in supersonic passages," Aerosp. Sci. Technol. **139**, 108404 (2023).
[16]N. Mushtaq and P. Gaetani, "Understanding and modeling unstarting phenomena in a supersonic inlet cascade," Phys. Fluids **35**, 106101 (2023).
[17]J. Sousa and G. Paniagua, "Entropy minimization design approach of supersonic internal passages," Entropy **17**, 5593 (2015).
[18]N. Mushtaq, G. Persico, and P. Gaetani, "The role of endwall shape optimization in the design of supersonic turbines for rotating detonation engines," J. Turbomach. **145**, 081015 (2023).
[19]D. Shen, M. Cheng, K. Wu, Z. Sheng, and J. Wang, "Effects of supersonic nozzle guide vanes on the performance and flow structures of a rotating detonation combustor," Acta Astronaut. **193**, 90–99 (2022).
[20]J. Sousa, G. Paniagua, and J. Saavedra, "Aerodynamic response of internal passages to pulsating inlet supersonic conditions," Comput. Fluids **149**, 31–40 (2017).
[21]N. Mushtaq and P. Gaetani, "The effect of upstream unsteadiness on the unstarting of a supersonic inlet turbine," J. Turbomach. **146**, 041005 (2023b).
[22]Z. Liu, J. Braun, and G. Paniagua, "Characterization of a supersonic turbine downstream of a rotating detonation combustor," J. Eng. Gas Turbines Power **141**, 031501 (2019).
[23]L. Su, F. Wen, C. Wan, J. Han, Y. Wang, and S. Wang, "Coupling study of supersonic turbine stage and two-dimensional hydrogen/air rotating detonation combustor," Phys. Fluids **35**, 66125 (2023).
[24]L. Su, F. Wen, C. Wan, Z. Li, J. Han, S. Wang, and Z. Wang, "Large-eddy simulation study of rotating detonation supersonic turbine nozzle generated by the method of characteristics under oscillating incoming flow," Phys. Fluids **34**, 116119 (2022).
[25]H. F. S. Lui, T. R. Ricciardi, W. R. Wolf, J. Braun, I. Rahbari, and G. Paniagua, "Unsteadiness of shock-boundary layer interactions in a Mach 2.0 supersonic turbine cascade," Phys. Rev. Fluids **7**, 94602 (2022).
[26]Y. Zhao and R. D. Sandberg, "Using a new entropy loss analysis to assess the accuracy of RANS predictions of an high-pressure turbine vane," J. Turbomach. **142**, 081008 (2020).
[27]J. Kutz, S. Brunton, B. Brunton, and J. Proctor, *Dynamic Mode Decomposition: Data-Driven Modeling of Complex Systems* (SIAM, 2016).
[28]J. P. Williams, O. Zahn, and J. N. Kutz, "Sensing with shallow recurrent decoder networks," Proc. R. Soc. A **480**, 20240054 (2024).
[29]R. Agromayor, B. Müller, and L. O. Nord, "One-dimensional annular diffuser model for preliminary turbomachinery design," Int. J. Turbomach. Propul. Power **4**(3), 31 (2019).
[30]L. J. Goldman and M. R. Vanco, "Computer program for design of two-dimensional sharp-edged-throat supersonic nozzle with boundary-layer correction," Technical Report No. NASA-TM-X-2343 (NASA, 1971).
[31]T. Schonfeld and M. Rudgyard, "Steady and unsteady flow simulations using the hybrid flow solver AVBP," AIAA J. **37**, 1378–1385 (1999).
[32]P. D. Lax and B. Wendroff, "Difference schemes for hyperbolic equations with high order of accuracy," Commun. Pure Appl. Math. **17**, 381–398 (1964).
[33]F. Nicoud and F. Ducros, "Subgrid-scale stress modelling based on the square of the velocity gradient tensor," Flow, Turbul. Combust. **62**, 183–200 (1999).
[34]E. Collado Morata, N. Gourdain, F. Duchaine, and L. Y. M. Gicquel, "Effects of free-stream turbulence on high pressure turbine blade heat transfer predicted

by structured and unstructured LES," Int. J. Heat Mass Transfer **55**, 5754–5768 (2012).
[35]P. C. Nassini, A. Andreini, and M. D. Bohon, "Characterization of refill region and mixing state immediately ahead of a hydrogen-air rotating detonation using LES," Combust. Flame **258**, 113050 (2023).
[36]ANSYS, *ANSYS CFX-Solver Theory Guide* (ANSYS, 2023).
[37]M. C. Druguet and D. E. Zeitoun, "Influence of numerical and viscous dissipation on shock wave reflections in supersonic steady flows," Comput. Fluids **32**, 515 (2003).
[38]T. Barth and D. Jerspersen, "The design and application of upwind schemes on unstructured meshes," in 27th Aerospace Sciences Meeting, AIAA Paper No. AIAA 1989-366, 1989.
[39]F. R. Menter, "Two-equation eddy-viscosity turbulence models for engineering applications," AIAA J. **32**, 1598–1605 (1994).
[40]D. E. Paxson and A. Naples, "Numerical and analytical assessment of a coupled rotating detonation engine and turbine experiment," in 55th AIAA Aerospace Sciences Meeting, AIAA Paper No. AIAA 2017-1746, 2017.
[41]C. Sun, H. Zheng, Z. Li, N. Zhao, L. Qi, and H. Guo, "Effects of diverging nozzle downstream on flow field parameters of rotating detonation combustor," Appl. Sci. **9**, 4259 (2019).
[42]B. A. Rankin, M. L. Fotia, A. G. Naples, C. A. Stevens, J. L. Hoke, T. A. Kaemming, S. W. Theuerkauf, and F. R. Schauer, "Overview of performance, application, and analysis of rotating detonation engine technologies," J. Propul. Power **33**, 131–143 (2017).
[43]P. Strempfl, O. Dounia, D. Laera, and T. Poinsot, "Effects of mixing assumptions and models for LES of hydrogen-fueled rotating detonation engines," Int. J. Hydrogen Energy **62**, 1–16 (2024).
[44]E. Bach, P. Stathopoulos, C. O. Paschereit, and M. D. Bohon, "Performance analysis of a rotating detonation combustor based on stagnation pressure measurements," Combust. Flame **217**, 21–36 (2020).
[45]B. S. Stratford and G. S. Beavers, "The calculation of the compressible turbulent boundary layer in an arbitrary pressure gradient—A correlation of certain previous methods," Reports and Memoranda No. 3207 (Aeronautical Research Council Reports & Memoranda, 1959).
[46]P. Bradshaw and D. H. Ferriss, "Calculation of boundary-layer development using the turbulent energy equation: Compressible flow on adiabatic walls," J. Fluid Mech. **46**, 83–110 (1971).
[47]H. Choi and P. Moin, "Grid-point requirements for large eddy simulation: Chapman's estimates revisited," Phys. Fluids **24**, 11702 (2012).
[48]B. Martin, F. Duchaine, L. Gicquel, N. Odier, and J. Dombard, "Accurate inlet boundary conditions to capture combustion chamber and turbine coupling with large-eddy simulation," J. Eng. Gas Turbines Power **144**, 021007 (2022).
[49]B. J. McBride *et al.*, "NASA Glenn coefficients for calculating thermodynamic properties of individual species," Technical Report No. NASA/TP-2002-211556 (National Aeronautics and Space Administration, John H. Glenn Research Center 2002).
[50]W. Sutherland, "LII. The viscosity of gases and molecular force," London, Edinburgh, Dublin Philos. Mag. J. Sci. **36**, 507–531 (1893).
[51]T. J. Poinsot and S. K. Lelef, "Boundary conditions for direct simulations of compressible viscous flows," J. Comput. Phys. **101**, 104–129 (1992).
[52]G. Wang, F. Duchaine, D. Papadogiannis, I. Duran, S. Moreau, and L. Y. M. Gicquel, "An overset grid method for large eddy simulation of turbomachinery stages," J. Comput. Phys. **274**, 333–355 (2014).
[53]I. B. Celik, Z. N. Cehreli, and I. Yavuz, "Index of resolution quality for large eddy simulations," J. Fluids Eng. **127**, 949–958 (2005).
[54]ANSYS, *ANSYS TurboGrid Reference Guide* (ANSYS Inc., 2023).
[55]I. B. Celik, U. Ghia, P. J. Roache, C. J. Freitas, H. Coleman, and P. E. Raad, "Procedure for estimation and reporting of uncertainty due to discretization in CFD applications," J. Fluids Eng. **130**, 780011 (2008).
[56]A. Prasad, "Calculation of the mixed-out state in turbomachine flows," J. Turbomach. **127**, 564–572 (2005).
[57]S. Jakirlić and R. Maduta, ""Steady" RANS modeling for improved prediction of wall-bounded separation," AIAA J. **54**, 1803–1809 (2016).
[58]B. H. Saracoglu, G. Paniagua, J. Sanchez, and P. Rambaud, "Effects of blunt trailing edge flow discharge in supersonic regime," Comput. Fluids **88**, 200–209 (2013).
[59]R. D. Sandberg and V. Michelassi, "Fluid dynamics of axial turbomachinery: Blade- and stage-level simulations and models," Annu. Rev. Fluid Mech. **54**, 255–285 (2022).
[60]W. E. Moeckel, "Approximate method for predicting form and location of detached shock waves ahead of plane or axially symmetric bodies," Report No. NASA-TN-1921 (NASA, 1921).
[61]J. D. Anderson, *Modern Compressible Flow: With Historical Perspective, Aeronautical and Aerospace Engineering Series* (McGraw-Hill Education, 2003).
[62]W. Stewart, "Analysis of two-dimensional compressible-flow loss characteristics downstream of turbomachine blade rows in terms of basic boundary-layer characteristics," Technical Report No. NACA-TN-3515 (NACA, 1955).
[63]J. D. Coull, "Endwall loss in turbine cascades," J. Turbomach. **139**, 081004 (2017).
[64]T. Borcherding, C. Bode, M. Rosenzweig, P. J. Przytarski, J. Leggett, and R. D. Sandberg, "Entropy loss breakdown comparison for LES and RANS of a transonic compressor stage midspan section," in ASME Turbo Expo: Turbomachinery Technical Conference and Exposition, 2023.
[65]S. Lee, S. K. Lele, and P. Moin, "Interaction of isotropic turbulence with shock waves: Effect of shock strength," J. Fluid Mech. **340**, 225–247 (1997).
[66]J. P. Gostelow, "A new approach to the experimental study of turbomachinery flow phenomena," J. Eng. Power **99**, 97–105 (1977).
[67]R. J. Miller, R. W. Moss, R. W. Ainsworth, and C. K. Horwood, "Time-resolved vane-rotor interaction in a high-pressure turbine stage," J. Turbomach. **125**, 1–13 (2003).
[68]P. J. Schmid, "Dynamic mode decomposition of numerical and experimental data," J. Fluid Mech. **656**, 5–28 (2010).
[69]D. Sashidhar and J. N. Kutz, "Bagging, optimized dynamic mode decomposition for robust, stable forecasting with spatial and temporal uncertainty quantification," Philos. Trans. R. Soc., A **380**, 20210199 (2022).
[70]S. Hochreiter and J. Schmidhuber, "Long short-term memory," Neural Comput. **9**, 1735–1780 (1997).